Petroleum Science 23 (2026) 7169–7186

Contents lists available at ScienceDirect

Petroleum Science

journal homepage: www.keaipublishing.com/en/journals/petroleum-science

Original Paper

Physics-informed coordinate-mapping categorizations for deciphering pore geometry and seepage capacity in oil shales

Li-Jiao Wu [a], Wei Wang [b], Derek Elsworth [c], Jun Liu [a,*]

[a] Institute of New Energy and Low-Carbon Technology, Sichuan University, Chengdu, 610065, Sichuan, China
[b] Chongqing Huadi Resources and Environment Technology Co., Ltd., Chongqing, 401120, China
[c] Department of Energy and Mineral Engineering, Pennsylvania State University, University Park, PA 16802, USA

ARTICLE INFO

Article history:
Received 19 March 2026
Received in revised form
21 April 2026
Accepted 30 June 2026
Available online 6 July 2026

Edited by Min Li

Keywords:
Low-maturity oil shale
In-situ heating
Seepage capacity
Fractal dimension
Pearson correlation analysis

ABSTRACT

In-situ thermal upgrading significantly alters pore structure in low-maturity oil shales, yet the key mechanisms controlling this transformation remain to be defined. Deciphering pore geometry and seepage capacity is crucial, as they directly dictate the flow network connectivity and ultimate hydrocarbon recovery; however, systematic quantification of their dynamic anisotropic variations is currently lacking. We establish two novel two-dimensional coordinate mapping classification schemes based on geometric parameters extracted via machine learning. These represent a seepage capacity classification based on pore cross-sectional area (S) and perimeter (C), and a morphological classification based on circularity (*Circ.*) and aspect ratio (AR). Observations reveal a pronounced anisotropy in pore evolution. Bedding-normal (nominally vertical), both seepage capacity and morphological complexity follow non-monotonic trajectories driven by stress. Bedding-parallel (nominally horizontal), however, permeability decreases with the increasing number and proportion of low seepage capacity pores (L-SC), and the quantity of each morphological pore type increase continuously, although morphological complexity is diluted by newly formed simple pores. Fractal dimension (D) and Pearson correlation analysis further corroborate this anisotropy: throughout the heating process, D values in bedding-parallel direction (D_H) remains consistently higher than in bedding-normal direction (D_V). D values monotonically increase in the bedding-normal direction, showing a significant positive correlation with regular elongated pores; whereas bedding-parallel, D values fluctuate, exhibiting the strongest correlation with transitional pores. These newly established classification frameworks provide quantitative tools for characterizing the anisotropic evolution of pore architecture and offer theoretical support for efficient in-situ conversion of low-maturity oil shale.

© 2026 The Authors. Publishing services by Elsevier B.V. on behalf of KeAi Communications Co. Ltd. This is an open access article under the CC BY-NC-ND license (http://creativecommons.org/licenses/by-nc-nd/4.0/).

1. Introduction

Rising global energy demand is straining conventional oil and gas supplies and threatening long-term sustainable economic development worldwide (Syed et al., 2022; Xu et al., 2022; Xie et al., 2026). As a major unconventional energy resource, shale oil and gas has become strategically important for global energy security (Kang et al., 2020; Xu et al., 2022; Paul et al., 2025; Yan et al., 2026). The United States leads global shale oil and gas production shifting from a net oil importer to an exporter and achieving energy self-sufficiently (Wang et al., 2023; McMahon et al., 2024; Zou et al., 2024). China possesses the second-largest oil shale reserves worldwide, trailing the United States geological reserve of 720 billion tons (Liu et al., 2006, 2017). Nevertheless, China's substantial oil shale deposits are immature or of low-maturity in their thermal evolution (Hu et al., 2014; Liu et al., 2017), necessitating stimulation methods like in-situ heating to generate mobile hydrocarbons (Pik et al., 2001; Hu et al., 2020; Kang et al., 2020; Zhang et al., 2024a; Hou et al., 2026; Zhu et al., 2026). During in-situ heating, coupled physical-chemical reactions drastically alter the pore network (Z. Wang et al., 2021; He et al., 2022; Zhang et al., 2023; Guo et al., 2025; Cheng et al., 2026), such as kerogen and bitumen pyrolysis (Xie and Zhao, 2017; Zhao

* Corresponding author.
E-mail address: j.liu@scu.edu.cn (J. Liu).
Peer review under the responsibility of China University of Petroleum (Beijing).

https://doi.org/10.1016/j.petsci.2026.06.059
1995-8226/© 2026 The Authors. Publishing services by Elsevier B.V. on behalf of KeAi Communications Co. Ltd. This is an open access article under the CC BY-NC-ND license (http://creativecommons.org/licenses/by-nc-nd/4.0/).

and Kang, 2021), matrix dehydration (Lee et al., 2014; Su et al., 2022), and thermal expansion (Wu et al., 2019; Li et al., 2025). These structural transformations dictate the dynamic evolution of seepage capacity, which directly controls fluid migration and ultimate recovery efficiency (Kang et al., 2011; Tian et al., 2023; Xu et al., 2023; Li et al., 2024; Zhang et al., 2025). The timing, strength and polarity of these feedbacks on pore structures define the resulting dynamic evolution of the seepage capacity as a result of the heating process. Thus, quantifying these pore-related mechanisms is foundational for optimizing in-situ upgrading for low-maturity oil shale.

The recognition, characterization and classification of shale pore systems have emerged as a prominent research focal point to evaluate unconventional reservoirs. Various classification theories have been developed and applied to assess hydrocarbon storage and transport capabilities. Traditionally, pore systems are classified by size (e.g., the IUPAC standard - micropores, mesopores and macropores) (Sing, 1985; Rouquerol et al., 1994a, 1994b; Chen et al., 2025a), genetic spatial relationships (e.g., interparticle, intraparticle, and organic-matter pores) (Loucks et al., 2012), visual morphology (e.g., uniform-spherical, ink-bottle and slit-shaped pores) (Sing, 1982; Zhang et al., 2023), and connectivity (e.g., closed and open pores, or blind and throughgoing pores) (Rouquerol et al., 1994b; Zhang et al., 2021). While these schemes provide valuable insights, they exhibit inherent limitations for complex reservoir evaluation. Conventional classifications frequently adopt a unidimensional perspective—such as relying solely on pore size, which insufficiently captures the seepage capacity controlled by flow-path connectivity (Chen et al., 2025b). Rather, the interest in quantifying pore size should ultimately be driven by the need to evaluate the hydrocarbon storage and seepage properties. Furthermore, morphological classifications typically rely on subjective visual assessments, lacking universal applicability. To some extent, a rigorous, objective, and multi-dimensional quantitative classification system remains largely absent.

To address this gap, we establish two novel two-dimensional coordinate mapping classification schemes based on geometric parameters extracted via machine learning—perimeter (*C*), area (*S*), circularity (*Circ.*), and aspect ratio (*AR*). The first scheme maps *C* against *S* to quantify low, medium, and high seepage capacity pores (L-SC, M-SC, H-SC). The second scheme maps *Circ.* against *AR* to classify geometric shapes (from near-circular to complex irregular) in a fully quantitative manner. The primary advantage of these schemes lies in providing a foundational, quantitative framework that eliminates subjective bias in pore evaluation, improving applicability, reproducibility and comparability. By mathematically mapping morphological descriptors, these schemes directly bridge the gap between microscopic pore geometry and macroscopic fluid transport potential. Specifically, they offer an unprecedented advantage in quantitatively tracking dynamic structural transformations during thermal maturation, accurately evaluating changing seepage behaviors, and ultimately guiding the optimization of in-situ conversion efficiency in low-maturity shales. Utilizing these frameworks, we systematically quantify the anisotropic thermal evolution in low-maturity oil shale parallel and normal to bedding planes. Beyond that, unlike conventional studies that use fractal techniques merely for static reservoir evaluation (Wang et al., 2024; Yang and Liu, 2025), we dynamically employ the fractal dimension (*D*) and Pearson correlation analysis to explicitly reveal the evolutionary trajectories of anisotropic structural complexity during the in-situ thermal upgrading, as well as the underlying driving mechanisms of specific pore types. This research not only proposes a robust theoretical classification system but also applies it to reveal the anisotropic evolutionary laws of pores in oil shale, providing theoretical support for effective hydrocarbon recovery.

2. Materials and methodology

2.1. Sample preparation

The oil shale samples are procured from the Songliao Basin in northeastern China, specifically the Cretaceous Nenjiang Formation representing an abundant source rock reserve and a primary target for shale oil and gas exploration in the region (Kang et al., 2025; Li et al., 2026). Coring yielded specimens from a subsurface depth of ~500 m. The shale samples exhibit low maturity, with a vitrinite reflectance (R_o) value of 0.64% and a total organic carbon (TOC) content of 5.89%. Mineralogical composition, determined by X-Ray diffraction measurement (XRD), is dominated by quartz and clay minerals, with subordinate constituents comprising feldspar, carbonate and pyrite—the respective proportions are shown in Fig. 1. To investigate anisotropic properties, samples are carefully cut and polished into two principal orientations: perpendicular-to-bedding (designated as Vertical-V) and parallel-to-bedding (designated as Horizontal-H) (Fig. 2(a)). Herein, the samples for scanning electron microscope (SEM) observation were prepared with dimensions of 3–4 mm in length/width and ~0.5 mm in thickness.

2.2. Experimental and analytical methods

2.2.1. SEM imaging with in-situ heating

Fig. 2(b) exhibits the FE-SEM apparatus, equipped with a specialized in-situ heating stage. This serves to observe real-time microstructural changes under elevated temperature. The heating stage is composed of a silicon substrate, and attains precise temperature control by means of an external water chiller within a high-vacuum environment (3×10^{-3} Pa) to prevent oxidation of organic matter. As shown in Fig. 2(c), we heated samples from 25 to 100, 200, 300, 400 and 500 °C successively, with a gradual heating rate of 5 °C/min applied to avoid thermal shock. Each temperature is maintained for 2 h to ensure steady-state conditions and sufficient pyrolysis of organic matter within the sample. Throughout the thermal upgrading process, sequential SEM images of a pre-selected and fixed view region are continuously captured for both V and H samples (Fig. 2(d)), facilitating a consistent documentation of the dynamic evolution of the pore structure. In this work, four SEM areas were selected along both

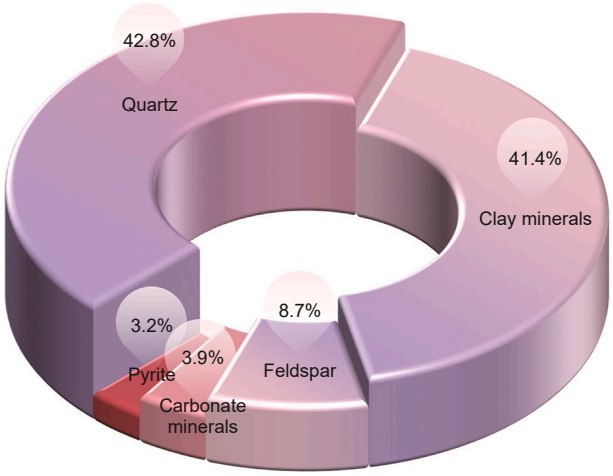


Fig. 1. Primary mineralogical composition of the oil shale samples.

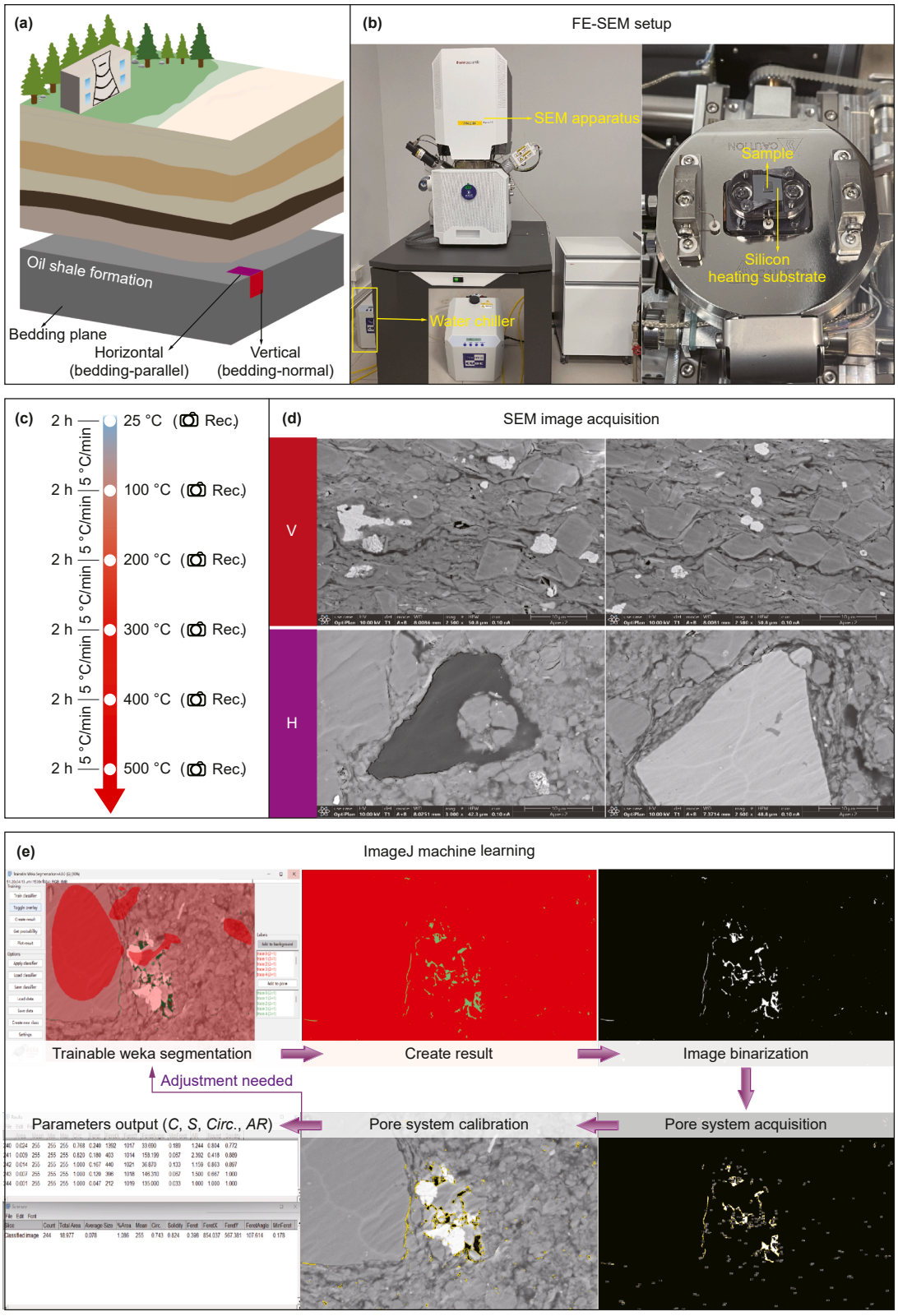


Fig. 2. In-situ heating and image processing workflow. **(a)** Orientation of the oil shale samples: bedding-normal (V) and bedding-parallel (H), **(b)** schematic of the field emission scanning electron microscopy (FE-SEM) apparatus with an in-situ heating stage and water chiller for temperature control, **(c)** programmed heating schedule, **(d)** acquisition of selected-view SEM images oil shale samples in V and H orientations, **(e)** image processing workflow using the Trainable Weka Segmentation (TWS) plugin in ImageJ software.

the H and V directions—representative examples are shown in Fig. 2(d).

2.2.2. Pore recognition and morphological parameterization

SEM images are subjected to digital processing through ImageJ software interfaced with the TWS plugin, a machine learning-driven tool for pixel-level classification, to obtain fine distinguishment of pore space from the solid matrix. The workflow is shown in Fig. 2(e). Prior to segmentation, image preprocessing is conducted using a non-local means filter to reduce background noise while strictly preserving the sharpness of pore boundaries. During the machine learning procedure, a Fast Random Forest classifier within the TWS plugin is utilized. The training set is established by manually annotating representative pixel regions across different gray-level thresholds into two distinct classes, viz., "Pore" and "Background". This is followed by an iterative pore identification phase, wherein repeated training and validation are conducted to optimize recognition accuracy. To eliminate digital artifacts and background noise, an extraction criterion is applied to discard isolated features with an area smaller than 1 pixel, which are considered below the effective resolution limit. Subsequently, automated parameter measurement is performed to quantify key morphological descriptors of the identified pores, including *C*, *S*, *Circ.* and *AR*. Mathematically, *S* is determined as the total pixel count within the pore converted to actual area units (μm^2), while *C* denotes the length of its outer boundary. *Circ.* is calculated as:

$$Circ. = \frac{4\pi S}{C^2} \tag{1}$$

with a value ranging from 0 to 1, where 1 represents a perfect circle. Aspect ratio (*AR*) is defined as the ratio of the major axis length to the minor axis length of the best-fit ellipse for each pore. The comprehensive digitization process for various pore types effectively converts visual SEM information into quantitative digital parameters, establishing a robust foundation for successive statistical analysis and classification of pore systems.

2.2.3. Seepage capacity characterization

The Hagen-Poiseuille model has been widely and reliably applied to quantify the seepage capacity in porous media (Godoy et al., 2025; Xiao et al., 2025; Zhou et al., 2026). Accordingly, the volumetric flow rate in a single capillary (q, $\mu m^3/s$) is,

$$q = \frac{\pi d_i^4}{128\mu} \times \frac{\Delta p}{L_H} \tag{2}$$

where Δp is the pressure difference (Pa), d_i is the capillary diameter (μm), L_H is the capillary length (μm) and μ is the fluid dynamic viscosity (Pa·s). The diameter of irregular oil shale pores is difficult to measure, thus being approximated using the concept of an equivalent hydraulic diameter (d_{ie}) of the flow channel (Gong and Qian, 2024), which is defined as,

$$d_{ie} = \frac{4S_i}{C_i} \tag{3}$$

where S_i (μm^2) and C_i (μm) are the cross-sectional area and perimeter of the *i*-th capillary, namely the area and perimeter of the *i*-th pore. As a result, substituting the equivalent hydraulic diameter (d_{ie}) for the capillary diameter (d_i) in Eq. (2) yields,

$$q = \frac{2\pi\left(\frac{S_i}{C_i}\right)^4}{\mu} \times \frac{\Delta p}{L_H} \tag{4}$$

Herein, all pore parameters are derived from 2D SEM observations, which cannot fully capture the full 3D pore geometry. To enable quantitative estimation of seepage capacity while acknowledging this limitation, we conceptually project the 2D SEM observed aperture into an idealized 3D flow channel by assigning it a unit thickness ($L = L_H = 1$ μm)—as if assuming the fluid is flowing through a very short channel while traversing this 2D pore cross-section (Fig. 3). Under the premise of an identical fluid medium (same viscosity) and pressure difference, Eq. (4) dictates that the volumetric flow rate through a single pore is predominantly determined by its hydraulic diameter. Since a higher volumetric flow rate under identical pressure conditions directly reflects greater seepage capacity, which is the fundamental physical implication of permeability (Zhang et al., 2024b), we select the fourth power of (S_i/C_i) as the evaluation index to evaluate the seepage capacity of an individual pore. As a result, the individual pore area (S_i) and perimeter (C_i), extracted via machine learning from the corresponding SEM image at each temperature, enable the estimation of the pore-scale seepage capacity in this work.

2.2.4. Fractal dimension (D) characterization

Fractal theory is employed to quantitatively characterize the complexity and heterogeneity of the pore structure (Dathe and Thullner, 2005; Zhang et al., 2018; Wu et al., 2022). Fractal dimension can be defined through multiple mathematical frameworks depending on the target of characterization, including the box-counting fractal dimension, the surface fractal dimension, the mass fractal dimension and the perimeter-area fractal dimension (L. Wang et al., 2021; Datseris et al., 2023; Silva et al., 2025). Among these, the perimeter-area fractal model is particularly suitable for 2D SEM derived pore morphologies, as it directly links pore boundary tortuosity and shape irregularity to fluid flow tortuosity and seepage resistance. This method could better reflect the actual geometric control on permeability in low-maturity shale during thermal treatment. *D* is determined based on the relationship between *C* and *S*, serving as a valuable parameter to characterize seepage behaviors in a porous medium more accurately, thereby elevating the prediction accuracy of permeability in low-permeability reservoirs during in-situ thermal treatment. According to fractal geometry, the perimeter-area relationship can be reformulated as (Liu et al., 2011; Qi et al., 2014):

$$\log C = \frac{D}{2}\log S + c_1 \tag{5}$$

where c_1 represents a constant intercept. This formulation establishes that for a fractal pore structure, a log-log plot of *C* against *S* should exhibit a linear relationship, with the slope of the best-fit

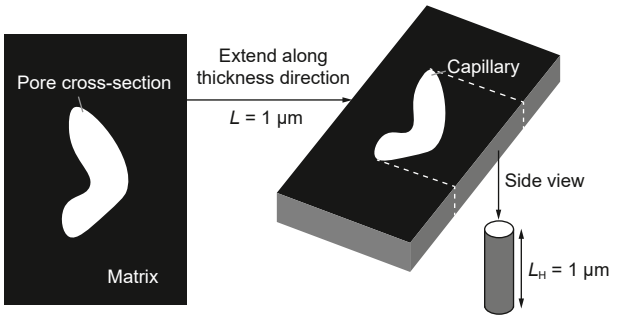


Fig. 3. Hypothetical 3D flow channel from 2D SEM imaging.

line equal to $D/2$. The D value is subsequently calculated as twice the slope value obtained from linear regression analysis of the log C versus log S data. To ensure absolute objectivity and avoid manual selection errors, the linear regression is automatically executed using the ordinary least-squares method encompassing the entire dataset of extracted pores at each temperature stage. D strictly range between 1 and 2, and a value approaching $D = 1$ implies a perfectly smooth, circular pore geometry, whereas a value approaching $D = 2$ corresponds to increasingly complex, highly tortuous pore boundaries that exert greater resistance to fluid flow.

3. Results

The morphological and seepage capacity parameters of pores, including C, S, *Circ.* and *AR*, are systematically extracted from the high-resolution FE-SEM images at 25 °C using the machine learning-aided segmentation workflow (Fig. 2(e)). To transform these quantitative descriptors into a structured and interpretable framework for pore system characterization, two novel two-dimensional coordinate-based classification schemes are established.

3.1. Seepage capacity (SC) coordinate mapping categorization

Based on the Hagen-Poiseuille model, the seepage capacity of an individual pore is evaluated, wherein the volumetric flow rate is proportional to the fourth power of the hydraulic diameter under identical pressure conditions. Since the hydraulic diameter for an irregular pore cross-section can be approximated as $d_{ie} = 4S_i/C_i$, the parameter $(S_i/C_i)^4$ serves as a direct proxy for the pore-scale seepage capacity (Eq. (4)). To establish a quantitative hierarchy, we select 3735 pore samples identified from the initial state (25 °C) FE-SEM images. By plotting these samples on a log-log coordinate system of S versus C, five isolines representing constant $(S/C)^4$ values are drawn to delineate boundaries (Fig. 4). Based on the clustering characteristics of the sample data and the distribution density, two critical thresholds are determined: $(S/C)^4 = 1 \times 10^{-6}$ and $(S/C)^4 = 1 \times 10^{-5}$, aiming to capture the inherent inflection points of flow potential across the pore network. Consequently, the pores are classified into three distinct categories: 1) Low seepage capacity pores (L-SC): defined by $(S/C)^4 < 1 \times 10^{-6}$, 2) Medium seepage capacity pores (M-SC): defined by $1 \times 10^{-6} \leq (S/C)^4 < 1 \times 10^{-5}$, 3) High seepage capacity pores (H-SC): defined by $(S/C)^4 \geq 1 \times 10^{-5}$; more detailed descriptions about various pore types are shown in Table 1.

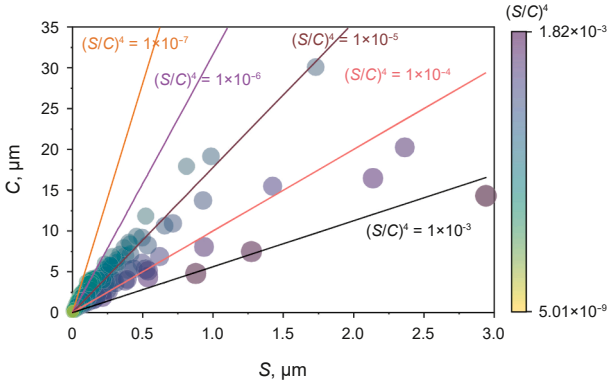


Fig. 4. Coordinate mapping classification of pore seepage capacity based on the relationship between S and C.

Table 1
Seepage capacity (SC) classification scheme.

Pore type	$(S/C)^4$ threshold	Description
L-SC	$(S/C)^4 < 1 \times 10^{-6}$	Pores with minimal contribution to fluid flow; typically, isolated micropores or pores with high specific surface area
M-SC	$1 \times 10^{-6} \leq (S/C)^4 < 1 \times 10^{-5}$	Pores with moderate flow potential; serve as transitional channels connecting storage spaces
H-SC	$(S/C)^4 \geq 1 \times 10^{-5}$	Pores with significant seepage capacity; mainly larger pores or fractures that dominate the macroscopic permeability

Based on the preset classification threshold, Fig. 5 shows the S-C log-log scatter plots in both vertical and parallel bedding directions at 25 °C, along with the percentage distribution of the three different pore types. In the V direction (Fig. 5(a)), the pore system is overwhelmingly dominated by L-SC pores, accounting for approximately 67.29% of the total count, while H-SC pores constitute a negligible fraction that account for less than 5%. Conversely, in the H direction (Fig. 5(b)), although L-SC pores still comprise the majority, the proportion of M-SC and H-SC pores is relatively lower compared to the V direction. This discrepancy at the initial state (25 °C) indicates that the native pore structure is strongly heterogeneous and governed by sedimentary bedding features. The relatively lower abundance of seepage-favorable pores (M-SC and H-SC) in the H direction suggests that, prior to thermal fracturing, the bedding planes are tightly compacted and do not yet serve as open seepage channels; instead, the dense arrangement of clay minerals and solid kerogen along these planes creates a barrier (He et al., 2022). At ambient temperature, the potential horizontal flow paths are effectively sealed by in-situ stress, consistent with the widely accepted understanding that pre-existing fractures contribute minimally to seepage until thermally activated (Burnham, 2017; Kang et al., 2011). Consequently, regardless of orientation, the oil shale at 25 °C is characterized by high storage capacity because of abundant L-SC pores but extremely poor connectivity, highlighting the critical necessity of in-situ heating to generate the internal pressure with thermal fracturing required to transform these isolated storage spaces into a connected flow network, to activate seepage capacity.

3.2. Morphological coordinate mapping categorization

We establish a robust morphological classification scheme based on two fundamental geometric parameters: *Circ.* and *AR* to quantitatively analyze pore morphological complexity. To determine scientifically sound classification thresholds, we calculate the theoretical circularity values of standard basic geometric shapes according to Eq. (1) (Table 2). Considering the resolution of the SEM images and the tolerance for pore edge detection, we set the critical thresholds as follows.

1) Set *Circ.* = 0.85 as the lower limit for near-circular pores, which is slightly lower than that of a regular hexagon (0.91) but higher than a square (0.785), accommodating pores that are visually round but possess slight edge angularity.
2) Set *Circ.* = 0.6 as the boundary between regular and irregular/transitional shapes, which approximates the circularity of an equilateral triangle, and below which the pore edges become significantly rough or the shape becomes highly distorted.

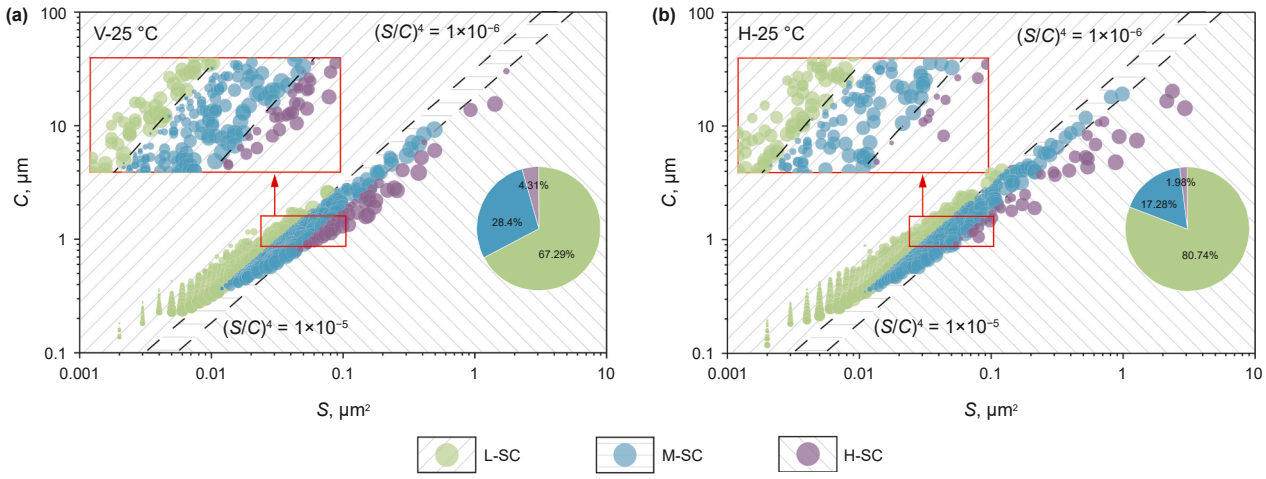


Fig. 5. SC classification template established based on *S* and *C* and statistical proportions of three seepage capacity pore types at 25 °C. **(a)** V direction, **(b)** H direction.

Table 2
Theoretical circularity values of standard basic geometric shapes used for threshold determination.

Geometric shape	Theoretical circularity	Classification threshold reference
Perfect circle	1.0	Upper limit
Regular octagon	≈0.95	/
Regular hexagon	≈0.91	0.85 (lower limit for near-circular)
Regular pentagon	≈0.86	/
Square	≈0.785	/
Equilateral triangle	≈0.60	0.6 (boundary for regular/irregular)

Table 3
Morphological classification scheme.

Pore type	*AR* threshold	*Circ.* threshold	Morphological description
Near-circular	$AR < 1.5$	$0.85 \leq Circ.$	Close to circular, smooth boundaries
Sub-circular	$AR < 1.5$ $1.5 \leq AR < 2.5$	$0.6 \leq Circ. < 0.85$ $0.6 \leq Circ.$	Slightly deviated from circular or short-axis, relatively regular
Transitional	$AR < 2.5$ $2.5 \leq AR < 5$	$0.4 \leq Circ. < 0.6$ $0.4 \leq Circ.$	Intermediate state between regular and irregular
Regular elongated	$AR \geq 5$	Any *Circ.*	Significantly elongated, similar to microfractures or bedding seams, exhibiting directionality
Complex irregular	$AR < 5$	$Circ. < 0.4$	Extremely irregular, complex edges, high tortuosity

3) Set $Circ. = 0.4$ as the threshold for complex pores, representing extremely irregular boundaries.
4) $AR = 1.5$, 2.5, and 5 are used to distinguish between blocky, short-columnar, and fracture-like pores. Specifically, $AR \geq 5$ is defined as the criterion for slit-shaped fractures.

As shown in Table 3, based on the combination of these quantitative thresholds, the pore system is categorized into five distinct morphological types: near-circular, sub-circular, transitional, regular elongated, and complex irregular pores.

Applying this scheme to the sample at 25 °C, the statistical results (Fig. 6) show that, in the V direction (Fig. 6(a)), the pore system is overwhelmingly dominated by sub-circular and near-circular pores. These two regular pore types collectively account for approximately 60.93% of the total number, with sub-circular pores alone constituting 42.9%. This distribution indicates that the native pore structure in the vertical cross-section consists primarily of interparticle or intracrystalline pores within the clay matrix, which have maintained relatively equiaxed shapes under overburden pressure (Loucks et al., 2012; Wang et al., 2023). Complex irregular pores also occupy a notable proportion, reflecting the inherent roughness of grain edges (Loucks et al., 2012). In the H direction (Fig. 6(b)), while the dominance of sub-circular pores persists, a subtle morphological differentiation is observed. The proportion of regular elongated pores, although low in absolute numbers at this immature stage, is comparatively higher than that in the V direction. This discrepancy suggests that even prior to thermal fracturing, the intrinsic bedding planes impose a directional control on pore geometry, creating flattened or slit-like precursors along the horizontal interfaces. Overall, the scarcity of macroscopic pores in both directions confirms that the low-maturity oil shale at 25 °C is characterized by a matrix-storage-dominated system rather than a pore-seepage-dominated one, providing a quantitative baseline for tracking the subsequent thermal evolution.

4. Discussion

4.1. Pore system evolution with increasing temperature

The total quantity of identified pores exhibits an overall increasing trend with rising temperature in both V and H directions (Fig. 7). From 25 to 300 °C, the number of pores increases mildly due to matrix dehydration shrinkage and initial microcrack formation (Lee et al., 2014). A sharp surge follows between 300 and 400 °C for pores in the H direction, driven by kerogen pyrolysis generating numerous organic nanopores (Hu et al., 2020). Crucially, a distinct decline occurs around 300–400 °C in the V direction. This non-monotonic behavior is governed by the synergistic effects of thermal stress, organic matter decomposition, and bedding-controlled structural heterogeneity. It is attributed not only to the bitumen blocking effect (He et al., 2022; Fan et al.,

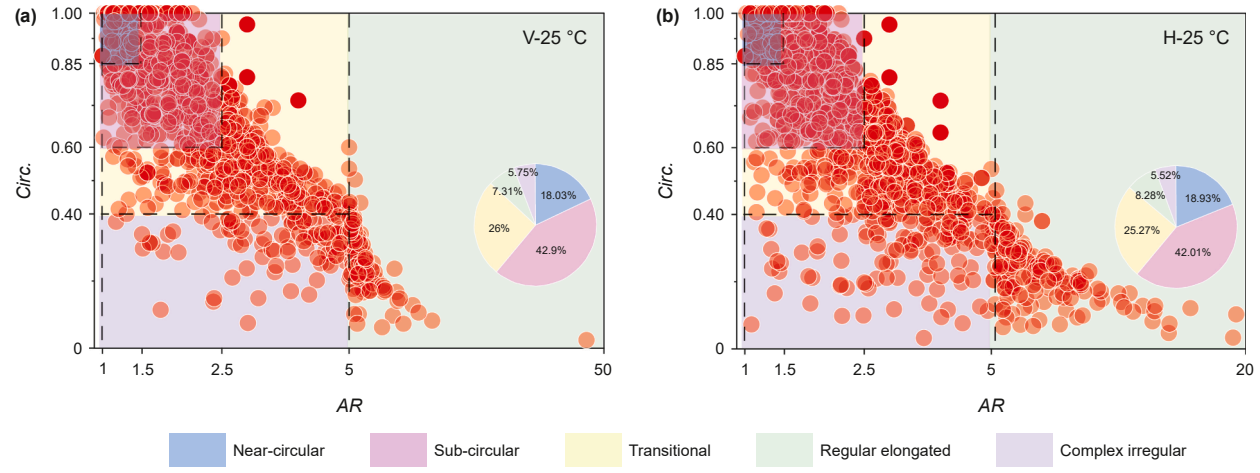


Fig. 6. Morphological classification template established based on *Circ.* and *AR* and statistical proportions of five pore types at 25 °C. **(a)** V direction, **(b)** H direction.

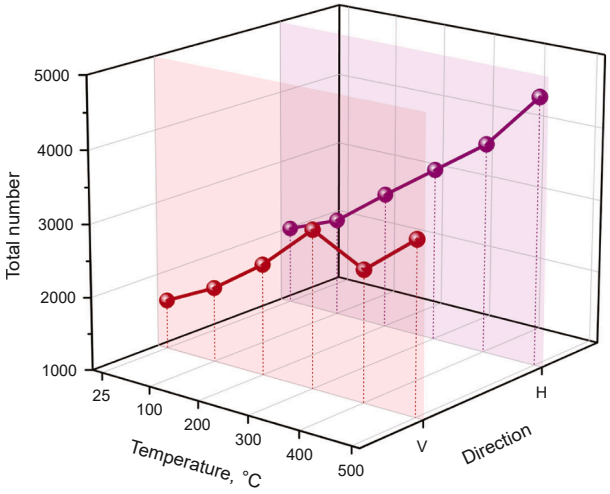


Fig. 7. Evolution of pore quantity with increased temperature.

2024; Zhu et al., 2025) where the generated viscous bitumen swells and fills the newly formed small pores, rendering them undetectable in SEM analysis, but also to pore coalescence (Chandra et al., 2021; Zhu et al., 2025; Guo et al., 2026) where the thin walls between adjacent micropores collapse as pyrolysis intensifies, causing multiple isolated small pores to merge into fewer, larger interconnected pores or microfractures, thus reducing the total count while enlarging individual volumes. Beyond 400 °C, the pore quantity rises again as bitumen volatilizes into gas and extensive thermal fractures develop. Importantly, this evolution manifests differently in the V and H directions, reflecting the strong structural anisotropy of the oil shale.

To visually corroborate these statistical trends, sequential high-resolution SEM images directly capturing the pore morphology evolution are obtained in Fig. 8. The positions of the observation windows selected in the V and H directions are shown in Fig. 8(a) and (b). As demonstrated in the V direction (Fig. 8(c)), a long horizontal crack evolves from a "plugged" state at 25 °C to a "microcrack-connected" longer crack at 300 °C, and further to its "widest" expanded state at 400 °C. This sequence documents a pore coalescence process, characterized by a decrease in pore count alongside an increase in spatial connectivity. This is because that local thermal stress at elevated temperatures can overcome matrix tensile strength to connect adjacent cracks (Wang et al., 2026). Conversely, in the H direction (Fig. 8(d)), we have observed that cracks are constantly forming and spreading along the original tight edge of a mineral grain ("original edge"). This preferential cracking behavior is consistent with Chen et al. (2025b), who attributed such phenomena to differential thermal expansion between mineral phases. By 500 °C, continuous generation of new secondary micropores completely transforms the local matrix, reflecting a monotonic increase in pore quantity; this is driven by intensive kerogen pyrolysis along bedding planes (Huang et al., 2025; Li et al., 2025).

4.1.1. Evolution of seepage capacity distribution

According to the seepage capacity (SC) classification, the evolution of the pore system demonstrates a distinct multi-stage characteristic, progressively enhancing anisotropy, as visualized in the SC coordinate mapping (Fig. 9) and quantitative statistics (Fig. 10). Fig. 9 visually reveals that the vast majority of pores cluster densely in the L-SC zone, confirming a system dominated by storage-type micropores, while H-SC pores appear as sparse points in the upper-right region. The specific evolutionary paths in the vertical and horizontal directions diverge significantly.

In the V direction, from 25 to 300 °C, the number of seepage pores initially decrease in terms of proportion (Fig. 10(a)). While the absolute count of M-SC pores increases moderately from 474 to 504 (Fig. 10(b)), the L-SC pore proportion rises significantly (Fig. 10(a)), which results in a dense concentration of data points in the lower-left region of Fig. 9(a), attributed to matrix dehydration and generating numerous unconnected shrinkage micropores that dilute the share of effective channels. However, between 300 and 400 °C, Fig. 9(a) exhibits a clear upward migration of data points. Quantitively, the proportion of H-SC and M-SC pores rises, while the L-SC proportion declines (Fig. 10(a)). The number of L-SC pores drops, whereas M-SC and H-SC pores rise slightly—the number of M-SC pores rises from 504 to 506 and that of H-SC pores rises from 76 to 79 (Fig. 10(b)). This strongly supports a pore coalescence mechanism, where dense micropores merge into larger interconnected networks, effectively lifting the seepage capacity ceiling. This structural transition from L-SC storage spaces to M-SC/H-SC channels represents a critical flow regime transition. Analogous to multi-stage transport and fluid redistribution phenomena observed in tight and fractured reservoirs, the sudden enhancement of pore-scale connectivity physically reduces the threshold pressure gradient required for fluid mobilization (Wang et al.,

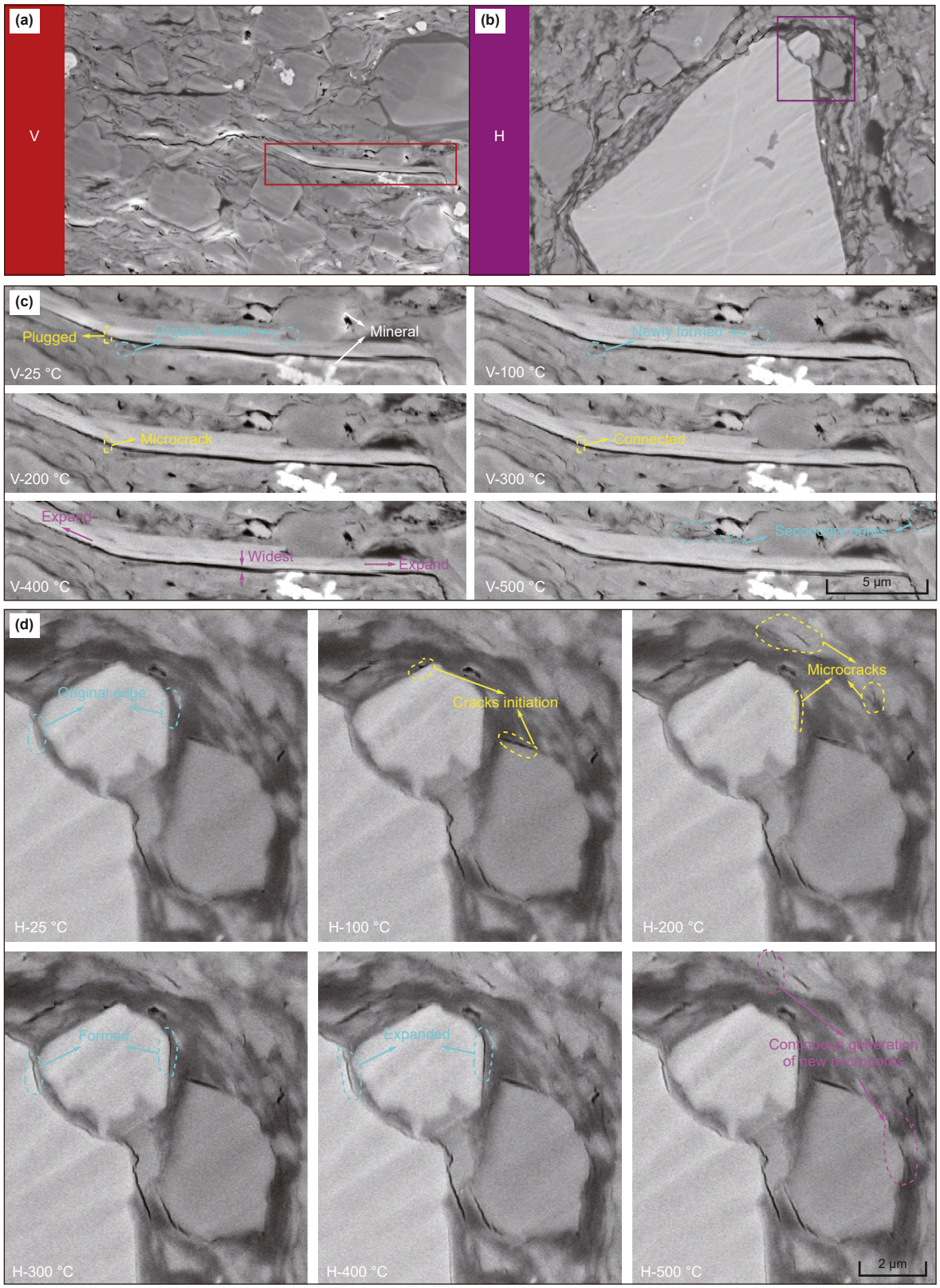


Fig. 8. In-situ sequential SEM images illustrating the distinct morphological evolution of pores and fractures during heating. **(a)** Selected imaging windows in the V direction, **(b)** selection imaging windows in the H direction, **(c)** evolution of a micro-channel in the V direction, **(d)** evolution of mineral edge separation and continuous generation of new micro-pores in the H direction.

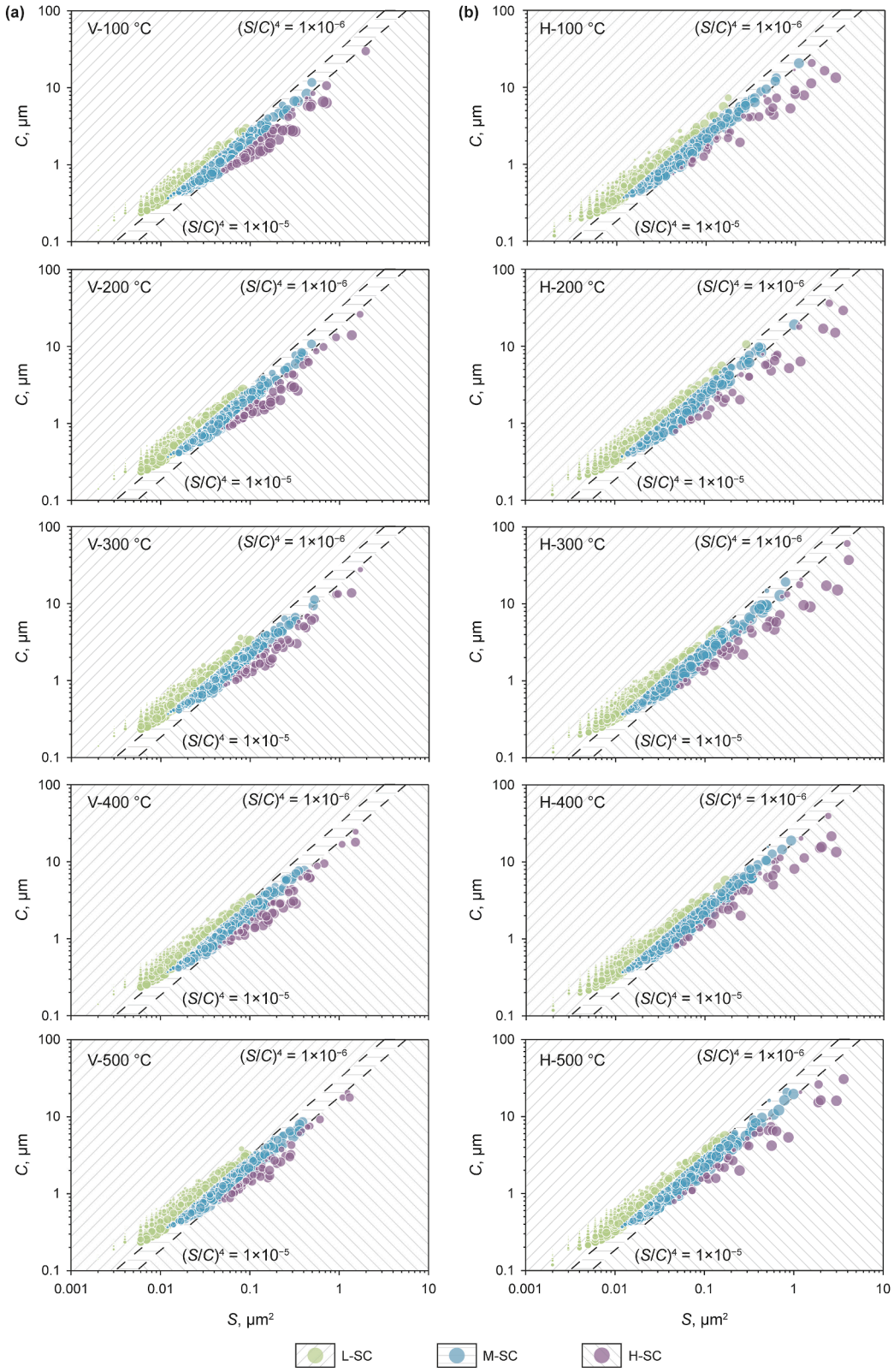


Fig. 9. Variation in SC coordinate mapping classification during heating operation. **(a)** V direction, **(b)** H direction.

2025; Cui et al., 2026). This dynamic staging dictates how the generated viscous bitumen and light hydrocarbons overcome capillary resistance to migrate from deep matrix to primary fracture networks (Nemčok et al., 2025). This improvement is reversed in the final stage (400–500 °C): the bottom of the L-SC zone becomes denser as shown in Fig. 9(a). Statistics show the proportion of H-SC and M-SC pores declines (Fig. 10(a)), with the H-SC pores number dropping to its minimum of 69, while the M-SC pores

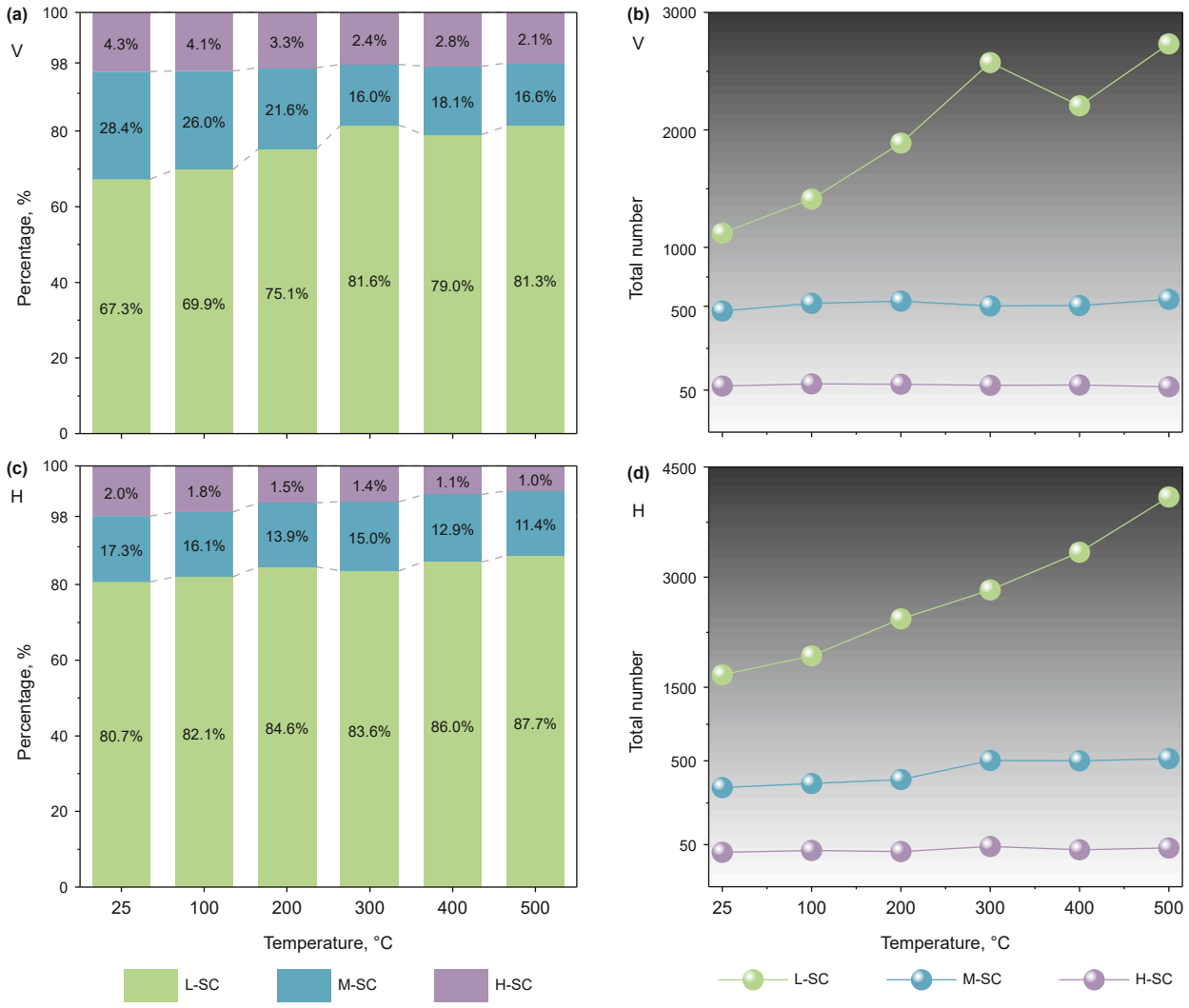


Fig. 10. Variation in percentage distribution and absolute number of three SC pore types for V direction **(a–b)** and H direction **(c–d)**.

number reaches 558 (Fig. 10(b)). The sharp rise in the number of L-SC pores (Fig. 10(b)) suggests that secondary cracking creates a massive number of tiny gas bubbles, which numerically dominate the pore system (Bernard et al., 2012; Guo et al., 2025), while some vertical fractures may close due to the overburden pressure (Ma et al., 2025).

However, the evolution in the H direction follows a different trajectory. A consistent decline in the H-SC pore proportion (Fig. 10(c)) attributes to that the number of L-SC pores rises continuously across the entire range (Fig. 10(d)). Fig. 9(b) shows a progressive thickening of the L-SC zone, indicating that the pyrolysis organic matter primarily acts as a source of nanopores along the bedding planes. A key divergence is observed in the M-SC pores: although their proportion fluctuates—decreasing from 25 to 200 °C, rising briefly at 200–300 °C, then declining again (Fig. 10(c)), their absolute count increases significantly from 357 at 25 °C to 530 at 500 °C (Fig. 10(d)). This reveals that while the seepage network is indeed expanding and connectivity is improving, the geometric proliferation of tiny L-SC pores is far faster, statistically masking this improvement. Furthermore, the absolute count of H-SC pores remains low and remarkably stable that it fluctuates between 41 and 48, with no sharp drop at high temperatures—from 44 at 400 °C to 46 at 500 °C (Fig. 10(d)). Unlike the vertical direction, horizontal bedding pores, once formed, are better preserved, maintaining a stable albeit sparse network of high-efficiency flow channels and severely regulating mass transfer and deep flow behavior during the in-situ thermal recovery process.

4.1.2. Evolution of morphological distribution

Complementing the seepage capacity assessment, the morphological classification provides deeper insights into the geometric transformation of the pore system, further elucidating the anisotropic evolution mechanisms during in-situ heating. In terms of commonalities, the coordinate mapping (Fig. 11) and quantitative statistics (Fig. 12) reveal that the pore systems in both V and H directions share a fundamental storage-dominated characteristic. Regardless of the orientation, the vast majority of pores cluster densely in the high-circularity zones, with near-circular and sub-circular pores consistently constituting the bulk of the pore space across all temperature stages—for V (Fig. 11(a)) and H direction (Fig. 11(b)). This indicates that matrix dehydration and organic matter pyrolysis universally generate spherical micropores as the primary storage space (He et al., 2022). Furthermore, broadly speaking, both directions exhibit a net expansion in pore quantity over the full heating range, reflecting the irreversible thermal degradation of the shale matrix (Yang et al., 2016; Burnham, 2017).

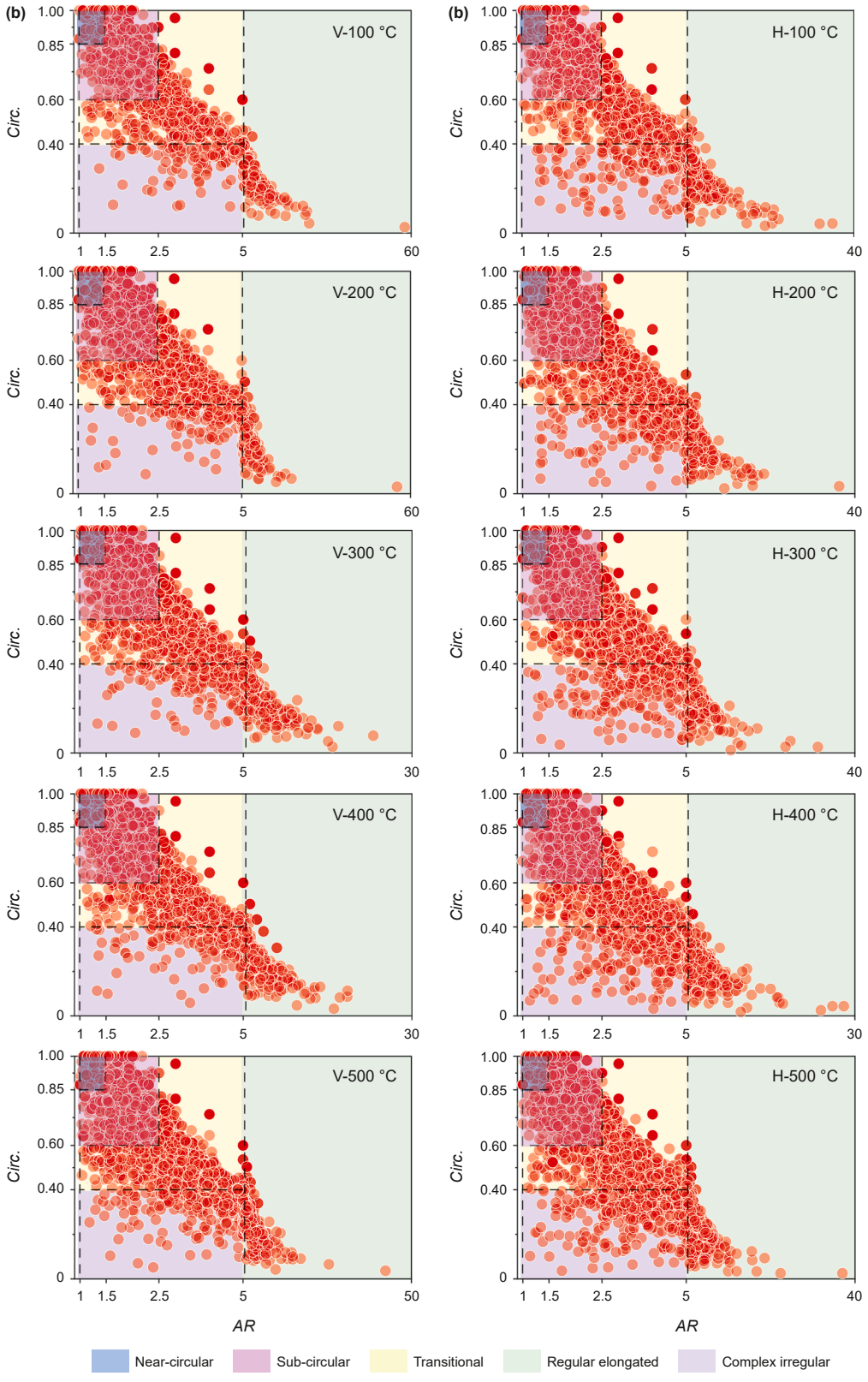


Fig. 11. Variation in morphological coordinate mapping classification during heating. **(a)** V direction, **(b)** H direction.

However, beneath these broad similarities lies a significant divergence during evolution, governed by the anisotropic response of the bedding structure to thermal stress. A sharp contrast appears in the intermediate temperature stage (300–400 °C). In the V direction, the evolution is non-monotonic (Fig. 12(a) and (b)). Contrary to the general trend of expansion, the number of all five types of pores decline significantly in this window (Fig. 12(b)). Concurrently, the proportion of regular elongated pores reaches a

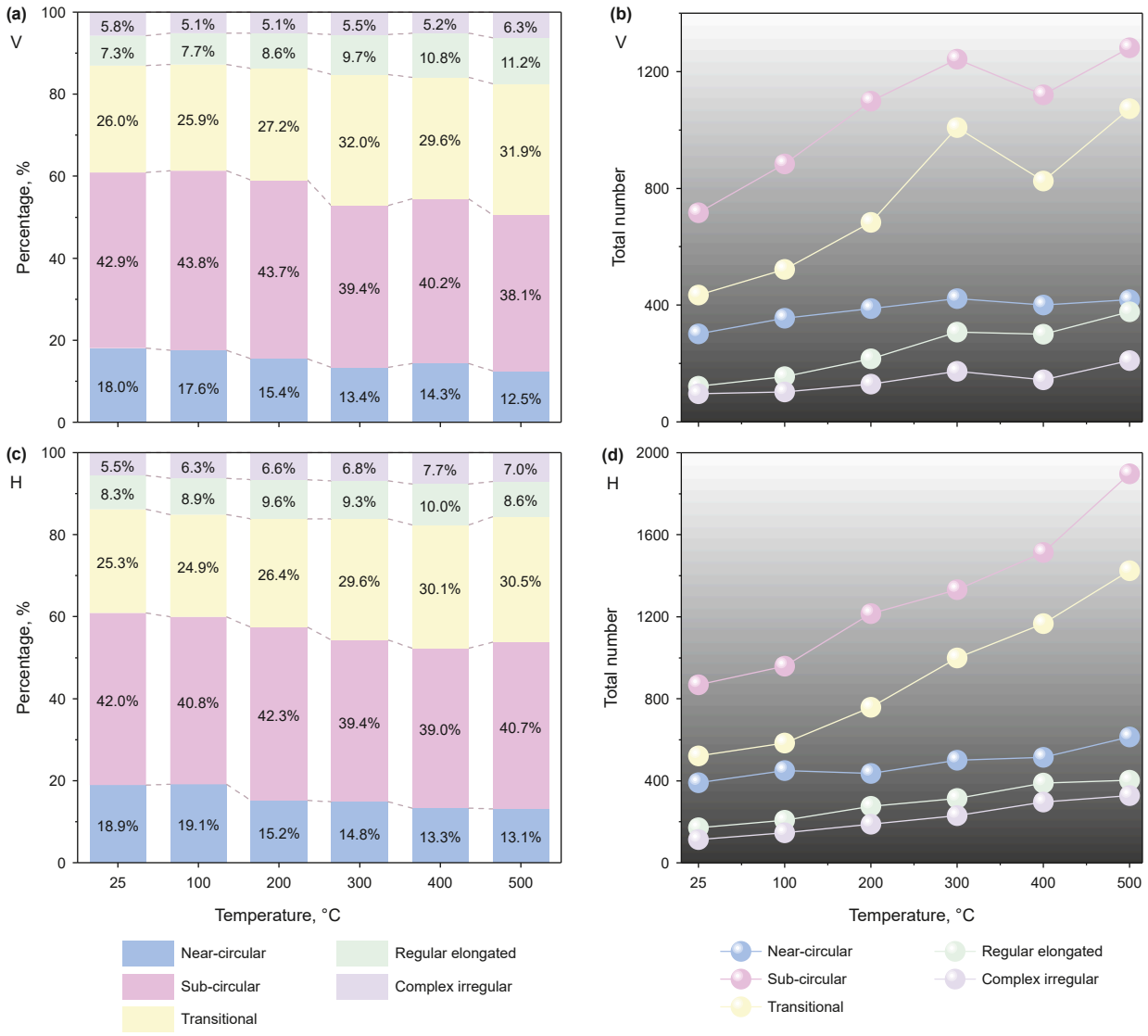


Fig. 12. Variation in percentage distribution and absolute number of five morphological pore types for V direction (**a**–**b**) and H direction (**c**–**d**).

local peak, rising from 9.7% to 10.8% (Fig. 12(a)). This reduction in small, simple pores accompanied by the relative enrichment of elongated pores provides compelling evidence that dense, isolated micropores are physically merging to form larger channels under the influence of vertical thermal stress. Conversely, the pores in the H direction follow a monotonic trend of continuous growth (Fig. 12(c) and (d)), largely immune to this reduction. The counts of almost all pore types rise steadily without interruption; for instance, sub-circular pores increase from 1216 to 1332, and transitional pores surge from 758 to 1000 in the same interval. This implies that along the bedding planes, the pore network evolves primarily through the continuous generation of new pores, driven by the laminated distribution of organic matter, rather than the complex merging process observed vertically. It can be inferred that the distinct horizontal lamination restricts thermal expansion predominantly to the vertical axis, thereby shielding the parallel-to-bedding structural defects from direct overburden compression. Consequently, pyrolysis-induced microfractures along horizontal interfaces are readily preserved and continually multiplied.

This anisotropy is further highlighted by the behavior of fracture-like pores under high-temperature conditions. In the H direction, although the relative proportion of regular elongated pores fluctuates between 8.3% and 10% (Fig. 12(c)), their number of regular elongated pores increases steadily and significantly from 171 at 25 °C to 403 at 500 °C (Fig. 12(d)), whose consistent number growth further indicates that horizontal bedding fractures act as preferential pathways that are better preserved against confining stress. In contrast, the V direction exhibits instability that the number of regular elongated pores stagnates and even slightly reduces from 307 at 300 °C to 300 at 400 °C before rising again (Fig. 12(b)). Consequently, the horizontal evolution is cumulative and stable, facilitating the sustained development of planar flow channels, whereas the vertical fractures are more sensitive to closure or deformation due to overburden pressure or clogging by residues from pyrolysis, resulting in a more dynamic and tortuous evolution of the vertical pore system.

4.1.3. Conceptual model development

To systematically synthesize the complex and anisotropic mechanisms in V and H directions, a conceptual evolution path model is proposed in Fig. 13. This model visually encapsulates the divergent trajectories of seepage capacity and morphological

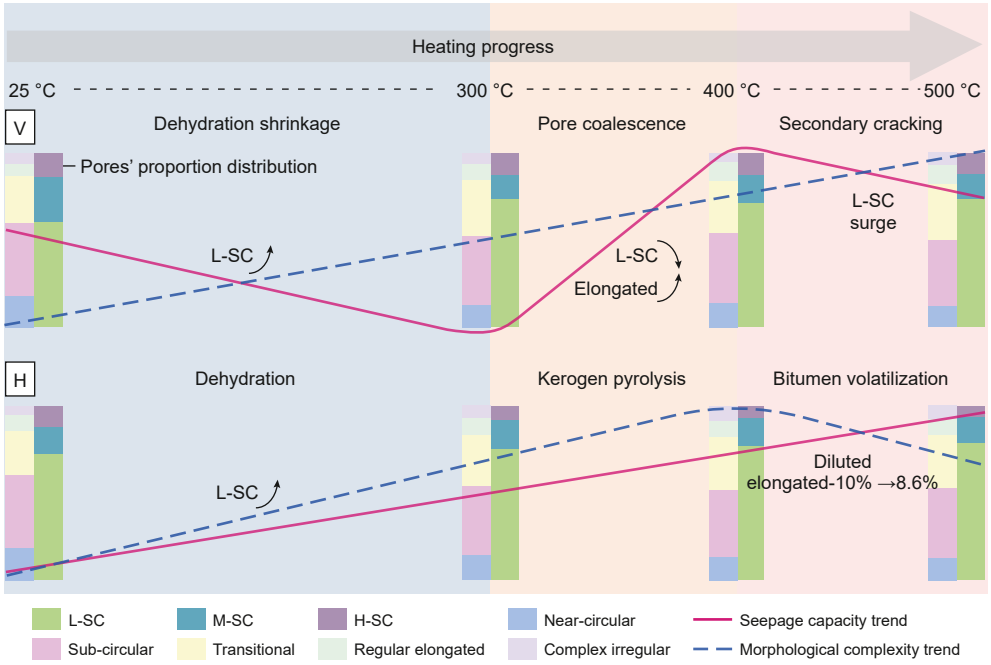


Fig. 13. Conceptual theoretical evolutionary path illustrating the anisotropic evolution patterns of pore systems in low-maturity oil shale reservoirs during in-situ heating.

complexity across heating stages. In the V direction, the process is fundamentally discontinuous: early dehydration shrinkage gives way to intense pore coalescence—causing the drop in L-SC pores and a spike in seepage capacity, followed by late-stage secondary cracking where massive generation of simple gas bubbles artificially dilutes the fracture proportion. Conversely, the H direction exhibits a highly continuous and cumulative evolution. Governed by the laminated organic matter distribution, kerogen pyrolysis and subsequent bitumen volatilization drive a relentless, monotonic proliferation of L-SC pores. Although high-efficiency horizontal fractures (elongated pores) are successfully generated and preserved, their statistical proportion is ultimately diluted by the sheer volume of newly formed nanopores. This comprehensive theoretical framework somewhat exhibits the intrinsic relationship between microscopic structural transformations and macroscopic seepage behavior during thermal upgrading.

4.2. Fractal characterization of pore structure complexity

4.2.1. Fractal dimension (D)

The fractal dimension (D), based on the measurements of S and C, is employed to quantitatively characterize the roughness of pore boundaries and the complexity of their geometry throughout thermal evolution. Herein, all the plots of log S versus log C for samples in both V and H directions demonstrate distinct and strong linear correlations in their distribution with correlation coefficients (R^2) consistently exceeding 0.95, as presented in Fig. 14. The calculated D values are summarized in Fig. 15.

The evolution of D reveals a striking anisotropic phenomenon. Across the entire temperature range, the D in the horizontal direction (D_H) is consistently higher than that in the vertical direction (D_V) (Fig. 15), indicating that the pore system along the bedding-parallel planes (H) inherently possesses lower uniformity of the pore size distribution, likely attributed to the heterogeneous, laminated distribution of organic matter and clay minerals (Ji et al., 2026). Anisotropically, D_V exhibits a continuous upward trend, whereas D_H displays a fluctuating pattern among sequentially increasing-then-decreasing. In the V direction, the continuous increase in D correlates strongly with the progressive shift from simple storage pores to complex fracture networks (Fig. 12(a) and (b)). Although the absolute count of L-SC pores fluctuates in Fig. 10(b), the morphological transformation dictates the complexity. As seen in Fig. 12(a), the proportion of simple pores declines steadily: near-circular pores drop from 18% at 25 °C to 12.5% at 500 °C and sub-circular pores from 42.9% to 38.1%. Conversely, the proportion of geometrically complex pores rises continuously: transitional pores increase from 26% to 31.9%, regular elongated pores from 7.3% to 11.2% and complex irregular pores from 5.8% to 6.3%. Even during the 300–400 °C stage where pore connection reduces the number of simple pores (Fig. 12(b)), the surviving pores are increasingly tortuous, and the proportion of regular elongated pores continues to rise (Fig. 12(a)). This suggests that, the thermal evolution of pore structure complexity is dominated by the propagation of vertical microcracks facilitating the interconnection of pores in the V direction, which irreversibly increases the surface roughness and geometric irregularity, thereby driving a continuous increase in the D value. In the H direction, during the 300–400 °C stage, D increases aligning with the peak development of pore complexity shown in Fig. 12(c), where the total proportion of geometrically complex pores reaches its maximum of 47.8%. Within this peak, both the regular elongated pores and the complex irregular pore types exhibit their individual maximum proportions simultaneously, 10% and 7.7% respectively. The reduction during the 400–500 °C stage can be explained by the rapid generation of simple pores. As shown in Fig. 10(d) and 12(d), the number of simple micropores (L-SC) and sub-circular pores surges drastically at 500 °C. Specifically, the number of sub-circular pores jumps from 1514 to 1897. This massive increase in smooth, round gas bubbles numerically overwhelms the number density of complex pores and fractures. Consequently, even though fractures still exist, their relative proportion drops (e.g., regular elongated falls from 10% to 8.6%, Fig. 12(c)). Since these new pores are geometrically simple and smooth, they lower the average roughness of the entire network, resulting in a final decrease in the D value.

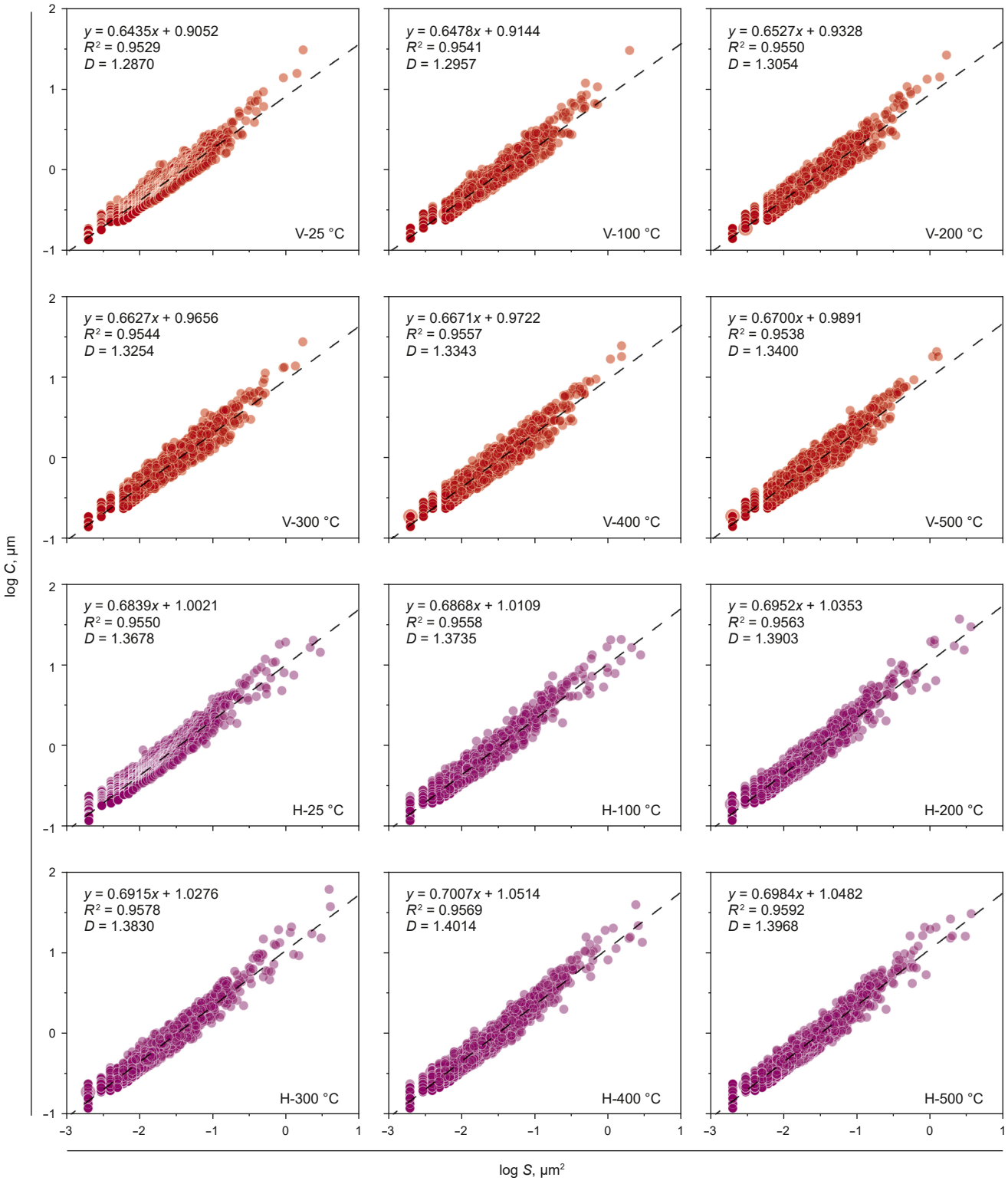


Fig. 14. Variation in log *C*-log *S* correlation determining fractal dimension (*D*) of the low-maturity oil shale pore structures at different temperatures.

Although the baseline positive correlation between geometric complexity and fractal dimension is well-documented in existing literature (Lü et al., 2019; Xiao et al., 2023), our results provide novel insights into how this relationship dynamically responds to temperature. The evolution of *D* fundamentally mirrors the competition between two thermally induced mechanisms. In the V direction, the continuous thermal propagation of microcracks completely dominates, irreversibly driving *D* upward. Conversely, in the H direction, the initial generation of complex interconnected channels is eventually numerically overwhelmed by the massive secondary generation of perfectly smooth gas bubbles at 500 °C, causing an anomalous structural simplification and a

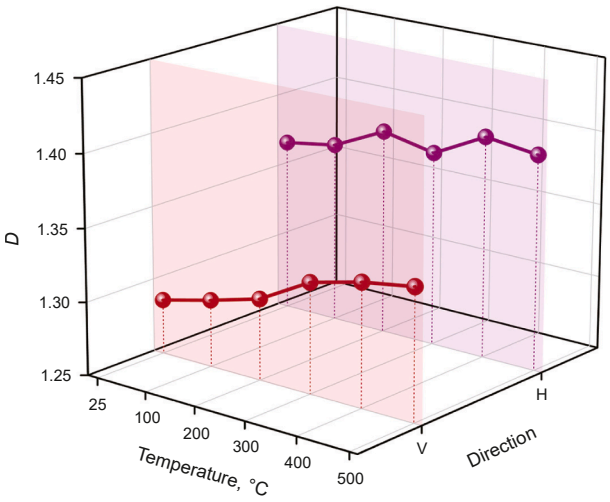


Fig. 15. Variation in fractal dimension (D) with temperature.

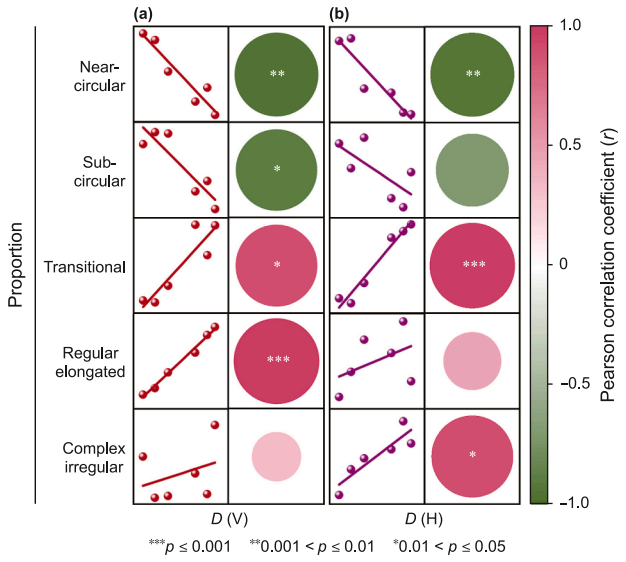


Fig. 17. Heatmap of correlation between pore type proportion and fractal dimension (D) in morphological classification scheme. **(a)** V direction, **(b)** H direction. The color gradient represents the Pearson correlation coefficient (r). Asterisks (*) denote the statistical significance level (p).

corresponding drop in D. This anisotropic, temperature-dependent fluctuation uniquely highlights the complexity of thermal upgrading in low-maturity oil shales.

4.2.2. Correlation between pore classification and D

We conduct Pearson correlation analysis between the fractal dimension (D) and the proportion of pore types defined by the seepage capacity and morphological classification schemes to identify the specific pore types driving the variation in fractal complexity. The results are presented as heatmaps in Figs. 16 and 17. In terms of seepage capacity (Fig. 16), the proportion of L-SC pores exhibits a positive correlation with D, whereas the M-SC and H-SC pores show a negative correlation. Notably, these correlations are stronger in the V direction (Fig. 16(a)) than in the H direction (Fig. 16(b)) implying that the vertical pore evolution is strictly governed by the accumulation of L-SC pores that significantly outpaces the development of large storage pores (Fig. 10(a)). The weaker correlation in the H direction is attributed to a decoupling effect that the simultaneous surge in both rough L-SC and smooth M-SC pores (e.g., M-SC count rising from 357 to 530, Fig. 10(d)) disrupts correlations based solely on size.

Regarding the morphological classification (Fig. 17), D exhibits a negative correlation with simple pores (near-circular and sub-circular) and a positive correlation with complex ones (transitional, regular elongated and complex irregular) in both directions. However, the dominant pore types differ significantly. In the V direction (Fig. 17(a)), the negative correlation with near-circular pores and the positive correlation with regular elongated pores are strongest and most significant, which aligns perfectly with the morphological evolution in Fig. 12(a), where the proportion of regular elongated pores continuously rises from 7.3% to 11.2% while near-circular pores decline from 18% to 12.5%. This confirms that the monotonic rise of D_V is dictated by the stress-induced propagation of vertical fractures. To the contrary, in the H direction (Fig. 17(b)), the transitional pores exhibit the highest correlation significance, while the relevance of regular elongated pores is lower than that in the V direction due to the previously mentioned decoupling. Although complex irregular pores show higher significance in the H direction, the massive influx of smooth sub-circular pores at 500 °C surges from 1514 to 1897 (Fig. 12(d)) and leads to a forced decline in the proportion of regular elongated pores. Therefore, the transitional type pores which bridge the gap between pores and fractures shows the strongest statistical tie to the D in the horizontal plane.

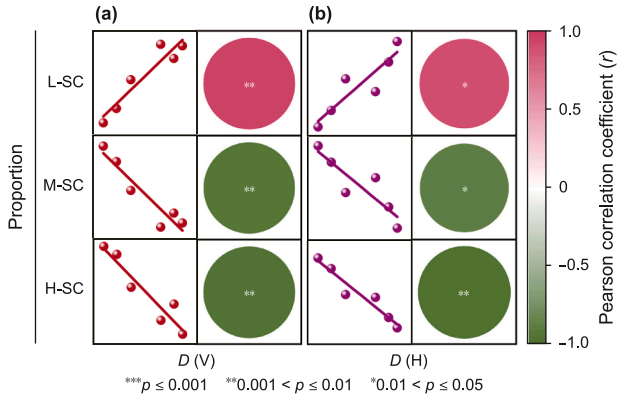


Fig. 16. Heatmap of correlation between pore type proportion and fractal dimension (D) in SC classification scheme. **(a)** V direction, **(b)** H direction. Color gradient represents the Pearson correlation coefficient (r). Asterisks (*) denote the statistical significance level (p).

4.3. Applications and advantages of the proposed classification frameworks

4.3.1. Engineering implications for in-situ thermal upgrading of low-maturity oil shale

Although the theoretical association between microscopic pore evolution and macroscopic seepage capacity has been widely recognized, its ultimate value lies in guiding the engineering optimization of low-maturity oil shale in-situ conversion. The proposed quantitative classifications, combined with fractal analysis, offer a robust petrophysical foundation for evaluating fluid migration, predicting permeability evolution, and optimizing field-scale thermal upgrading strategies. Firstly, the dynamic tracking of the SC classification directly serves as a proxy for permeability evolution. Our findings reveal that the formation of effective permeability is not a linear process. The critical flow regime transition where isolated L-SC pores coalesce into

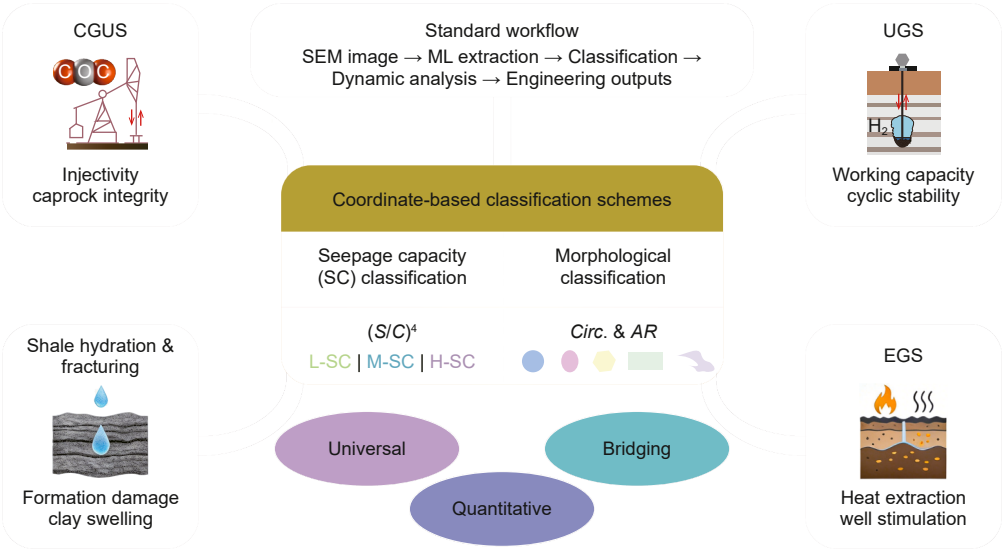


Fig. 18. Conceptual framework illustrating the broad applicability of the proposed pore classification schemes across diverse subsurface energy and environmental systems.

connected M-SC and H-SC pores predominantly occurs in the 300–400 °C. From an engineering perspective, this indicates that the target formation must be reliably heated beyond this temperature to successfully mobilize heavy bitumen and initiate deep fluid migration. Secondly, evaluating fluid migration resistance using morphological classification and fractal theory can help engineers design systems that enable hydrocarbons to flow and be recovered more efficiently along desired pathways within highly anisotropic shale formations. Finally, these microscopic insights suggest that blindly increasing the heating temperature may not yield proportionally higher fluid recovery. Instead, maintaining a steady optimal temperature phase (e.g., around 400 °C) might better preserve the structural integrity of the H-SC fracture network while minimizing unnecessary energy consumption, ultimately maximizing the overall economic feasibility of the in-situ upgrading process.

4.3.2. Potential of expandable application

Apart from oil shale, the principal advantage of these newly proposed coordinate-based mapping schemes lies in their decoupling from specific lithologies. This portable toolkit relies entirely on basic geometric descriptors (*C*, *S*, *Circ.*, *AR*) obtained through digital image analysis and demonstrates great potential for characterizing complex microstructural changes across a wide spectrum of subsurface energy and environmental systems (Fig. 18). Particularly in the field of CO_2 geological storage and utilization (CGUS), these frameworks can be employed to quantitatively track microstructural alterations of pores system induced by CO_2 injection. By applying the SC mapping, operators can distinguish whether CO_2-brine-rock reactions enhance flow pathways (shifting to H-SC/M-SC) or block them through mineral precipitation (shifting to L-SC). Simultaneously, morphological mapping could reveal whether CO_2-induced dissolution leads to uniform spherical enlargement or highly channelized, elongated fractures. Such quantitative insights directly inform critical engineering parameters, including injection sustainability, storage capacity and long-term sealing integrity.

Additionally, the frameworks are readily adaptable to other emerging domains, such as underground hydrogen storage (UGS) and enhanced geothermal systems (EGS). In UGS, the low viscosity and high diffusivity of hydrogen impose stringent requirements on pore connectivity and seepage efficiency. Repeated injection/withdrawal cycles may alter pore geometry and seepage efficiency - changes that can be systematically categorized using the proposed morphological and SC criteria to evaluate reservoir stability and cycling performance. In EGS, the evolution of fracture networks under thermo-hydro-mechanical-chemical forcings can be quantified to distinguishing between efficient flow conduits (aligned with H-SC/regular elongated pores) and inefficient or sealed fractures. This capability is essential for optimizing stimulation strategies and predicting long-term heat extraction performance. The frameworks, as a standardized workflow - from machine learning parameter extraction to dynamic mapping—enables a seamless translation from microscopic geometric observations to macroscopic field-scale performance predictions across diverse applications.

5. Conclusions

This study provides an alternate quantitative classification of the multiscale evolution of pore structure in low-maturity oil shale during in-situ thermal treatment. We use high-resolution FE-SEM imaging coupled with a machine learning-aided segmentation workflow. The main conclusions yielded are as follows.

By introducing pore perimeter, area, circularity, and aspect ratio, two novel coordinate-based classification schemes are newly established. The first is a seepage capacity (SC) classification differentiating effective flow channels (M-SC/H-SC) from storage spaces (L-SC), and the second a morphological classification distinguishing five pore shapes.

The thermal evolution exhibits pronounced anisotropy. In the bedding-normal (vertical) direction, the evolution of seepage capacity follows a non-monotonic trajectory—initial reduction, subsequent enhancement, and final decline. Morphological changes are dominated by pore coalescence at 300–400 °C, which is evidenced by a decrease in the pore count accompanied by a concurrent increase in the proportion of regular elongated pores. In the bedding-parallel (horizontal) direction, L-SC pores increase continuously while M-SC pores also rise in absolute number, forming a mixed-growth pattern; morphologically, all pore types show monotonic increases in count, although a large evolution of smooth sub-circular pores at 500 °C dilutes overall complexity.

The pore system along the bedding planes is inherently more complex than in the bedding-normal (vertical) direction ($D_H > D_V$). In this vertical direction, D rises monotonically correlating strongly with regular elongated pores, confirming fracture-driven growth in complexity. In the bedding-parallel (horizontal) direction, D fluctuates, peaking at 400 °C then declining at 500 °C, correlating most strongly with transitional pores.

The established classification schemes, based on fundamental geometric parameters rather than lithology-specific properties, offer broad applicability to other unconventional reservoirs. They bridge microscopic pore geometry with macroscopic transport behavior, providing a generalized framework for characterizing anisotropic pore evolution during thermal upgrading.

CRediT authorship contribution statement

Li-Jiao Wu: Writing – original draft, Visualization, Methodology, Data curation. **Wei Wang:** Resources, Investigation, Data curation. **Derek Elsworth:** Writing – review & editing, Methodology, Conceptualization. **Jun Liu:** Writing – review & editing, Writing – original draft, Supervision, Funding acquisition, Conceptualization.

Conflict of interest

The authors declare that the research was conducted in the absence of any commercial or financial relationships that could be construed as a potential conflict of interest.

Acknowledgements

This study was financially supported by the National Natural Science Foundation of China (Grant No. 42472239) and the Sichuan Science and Technology Program (Grant No. 2025YFHZ0077).

References

Bernard, S., Wirth, R., Schreiber, A., Schulz, H.-M., Horsfield, B., 2012. Formation of nanoporous pyrobitumen residues during maturation of the Barnett Shale (Fort Worth Basin). Int. J. Coal Geol. 103, 3–11. https://doi.org/10.1016/j.coal.2012.04.010.

Burnham, A.K., 2017. Porosity and permeability of Green River oil shale and their changes during retorting. Fuel 203, 208–213. https://doi.org/10.1016/j.fuel.2017.04.119.

Chandra, D., Bakshi, T., Vishal, V., 2021. Thermal effect on pore characteristics of shale under inert and oxic environments: insights on pore evolution. Microporous Mesoporous Mater. 316, 110969. https://doi.org/10.1016/j.micromeso.2021.110969.

Chen, S., Li, X., Zhu, G., Lu, Z., Wang, R., Huang, Y., Lan, W., Jia, F., Zhu, Y., 2025a. Classification, controlling factors, and multi-scale characterization techniques in shale reservoir pores: a comprehensive review. Gas Sci. Eng. 140, 205662. https://doi.org/10.1016/j.jgsce.2025.205662.

Chen, Z., Song, S., Zhang, W., Mei, S., Zhang, S., 2025b. Investigation of thermal-hydraulic-mechanical coupling model for in-situ transformation of oil shale considering pore structure and anisotropy. Eng. Geol. 344, 107859. https://doi.org/10.1016/j.enggeo.2024.107859.

Cheng, L., Xu, X., Gou, J., Liu, C., Han, K., Jiang, C., Liu, N., Meng, C., Liu, J., 2026. Cooling artifacts in ex-situ pore characterization of thermally stimulated low-maturity shale: an in-situ SEM imaging reassessment. Sci. Rep. 16, 4386. https://doi.org/10.1038/s41598-025-34434-0.

Cui, M., Lun, Z., Zhang, J., Niu, J., Xiao, P., 2026. Multiscale single-phase flow mechanisms of shale oil revealed by high-pressure nuclear magnetic resonance experiments. Fluid Dynam. Mater. Process. 22 (2), 9. https://doi.org/10.32604/fdmp.2026.075360.

Dathe, A., Thullner, M., 2005. The relationship between fractal properties of solid matrix and pore space in porous media. Geoderma 129 (3–4), 279–290. https://doi.org/10.1016/j.geoderma.2005.01.003.

Datseris, G., Kottlarz, I., Braun, A.P., Parlitz, U., 2023. Estimating fractal dimensions: a comparative review and open source implementations. Chaos: An Interdisciplinary Journal of Nonlinear Science 33 (10), 102101. https://doi.org/10.1063/5.0160394.

Fan, Q., Cheng, P., Gai, H., Yu, Z., Meng, G., Xiao, X., 2024. Effects of post-oil bitumen on the nanopore development of shales: new insights from a stepwise thermal simulation experiment on small shale plug samples. Mar. Petrol. Geol. 168, 107038. https://doi.org/10.1016/j.marpetgeo.2024.107038.

Godoy, P.A., Orujov, A., Gramatges, A.P., Aryana, S.A., 2025. Rock-on-a-chip: a novel method for designing representative microfluidic platforms based on real rock structures and pore network modelling. Lab Chip 25 (13), 3109–3122. https://doi.org/10.1039/D5LC00119F.

Gong, Y., Qian, Y., 2024. Deriving an unsaturated hydraulic conductivity function based on ergun equation. IOP Conf. Ser. Earth Environ. Sci. 1334, 012006. https://doi.org/10.1088/1755-1315/1334/1/012006.

Guo, Q., Sun, X., Wang, Y., Xu, C., Li, W., He, C., 2026. Temperature-dependent pore size redistribution and fractal complexity in low-maturity shale: implications for in situ conversion. Fractal and Fractional 10 (2), 132. https://doi.org/10.3390/fractalfract10020132.

Guo, W., Fan, C., Deng, S., Shui, H., Liu, Z., 2025. Secondary cracking characteristics of asphaltenes and insights into the reservoir unblocking during oil shale in-situ exploitation. Adv. Geo-Energy Res. 15 (1), 13–26. https://doi.org/10.46690/ager.2025.01.03.

He, W., Meng, Q.a., Lin, T., Wang, R., Liu, X., Ma, S., Li, X., Yang, F., Sun, G., 2022. Evolution features of in-situ permeability of low-maturity shale with the increasing temperature, Cretaceous Nenjiang Formation, northern Songliao Basin, NE China. Petrol. Explor. Dev. 49 (3), 516–529. https://doi.org/10.1016/S1876-3804(22)60043-0.

Hou, L., Ma, W., Mi, J., Xia, L., Ma, X., Liao, F., Lin, S., 2026. Multi-heating-rate pyrolysis study for modeling hydrocarbon production from in-situ conversion of Chang 7 shale. Sci. Rep. 16, 2106. https://doi.org/10.1038/s41598-025-31784-7.

Hu, M., Cheng, Z., Zhang, M., Liu, M., Song, L., Zhang, Y., Li, J., 2014. Effect of calcite, kaolinite, gypsum, and montmorillonite on Huadian oil shale kerogen pyrolysis. Energy & Fuels 28 (3), 1860–1867. https://doi.org/10.1021/ef4024417.

Hu, S., Zhao, W., Hou, L., Yang, Z., Zhu, R., Wu, S., Bai, B., Jin, X., 2020. Development potential and technical strategy of continental shale oil in China. Petrol. Explor. Dev. 47 (4), 877–887. https://doi.org/10.1016/S1876-3804(20)60103-3.

Huang, X., Yang, D., Wang, G., Zhang, K., Zhao, J., 2025. Evolution patterns and anisotropic connectivity characteristics of pores and fissures in oil shale after steam heating at different temperatures. Natural Resources Research 34, 409–425. https://doi.org/10.1007/s11053-024-10406-5.

Ji, Y., Grigore, M., Radlinski, A.P., Piane, C.D., Blach, T., Chen, X., Vu, P., Sun, M., Sakurovs, R., de Campo, L., Gilbert, E.P., Regenauer-Lieb, K., 2026. Nanopore structure characterization of Velkerri Shale: SANS investigation of pore accessibility and anisotropy. Fuel 403, 136079. https://doi.org/10.1016/j.fuel.2025.136079.

Kang, Y., Liu, K., Zhu, R., Zhang, S., Wu, S., Zhang, J., Liu, C., 2025. Origin and evolution of clay mineral and its impact on shale oil enrichment: insight from Qingshankou Formation, Songliao Basin, NE China. ACS Omega 10 (49), 60252–60269. https://doi.org/10.1021/acsomega.5c06337.

Kang, Z., Yang, D., Yangsheng, Z., Hu, Y., 2011. Thermal cracking and corresponding permeability of Fushun oil shale. Oil Shale 28 (2), 273–283. https://doi.org/10.3176/oil.2011.2.02.

Kang, Z., Zhao, Y., Yang, D., 2020. Review of oil shale in-situ conversion technology. Appl. Energy 269, 115121. https://doi.org/10.1016/j.apenergy.2020.115121.

Lee, S., Fischer, T.B., Stokes, M.R., Klingler, R.J., Ilavsky, J., McCarty, D.K., Wigand, M.O., Derkowski, A., Winans, R.E., 2014. Dehydration effect on the pore size, porosity, and fractal parameters of shale rocks: ultrasmall-angle X-ray scattering study. Energy & Fuels 28 (11), 6772–6779. https://doi.org/10.1021/ef501427d.

Li, L., Tang, X., Zhou, X., Chen, X., Chen, Q., Yan, H., Yan, Z., 2025. Experimental study on the improvement of micro-pore structure in medium-low maturity continental oil shale by temperature alteration. Sci. Rep. 15, 7706. https://doi.org/10.1038/s41598-025-90784-9.

Li, M., Wang, M., Zhang, L., Wang, Q., Wang, X., Li, X., Deng, Z., Dong, S., 2024. Understanding pore space and oil content of liquid-rich shale in the southern Bohai Sea, China. Geoenergy Sci. Eng. 233, 212552. https://doi.org/10.1016/j.geoen.2023.212552.

Li, Y., Song, Y., Xiong, B., Zhong, J., 2026. Sedimentary and hydrodynamic controls on shale oil sweet spots: a new storm deposition model for the Gulong Sag, Songliao Basin. Energies 19 (5), 1142. https://doi.org/10.3390/en19051142.

Liu, C., Hendriksen, M.W., Hutt, D.A., Conway, P.P., Whalley, D.C., 2006. Materials and processes issues in fine pitch eutectic solder flip chip interconnection. IEEE Trans. Compon. Packag. Technol. 29 (4), 869–876. https://doi.org/10.1109/TCAPT.2006.885973.

Liu, C., Shi, B., Zhou, J., Tang, C., 2011. Quantification and characterization of microporosity by image processing, geometric measurement and statistical methods: application on SEM images of clay materials. Appl. Clay Sci. 54 (1), 97–106. https://doi.org/10.1016/j.clay.2011.07.022.

Liu, Z., Meng, Q., Dong, Q., Zhu, J., Guo, W., Ye, S., Liu, R., Jia, J., 2017. Characteristics and resource potential of oil shale in China. Oil Shale 34 (1), 15–41. https://doi.org/10.3176/oil.2017.1.02.

Loucks, R.G., Reed, R.M., Ruppel, S.C., Hammes, U., 2012. Spectrum of pore types and networks in mudrocks and a descriptive classification for matrix-related mudrock pores. AAPG (Am. Assoc. Pet. Geol.) Bull. 96 (6), 1071–1098. https://doi.org/10.1306/08171111061.

Lü, Q., Qiu, Q., Zheng, J., Wang, J., Zeng, Q., 2019. Fractal dimension of concrete incorporating silica fume and its correlations to pore structure, strength and

permeability. Constr. Build. Mater. 228, 116986. https://doi.org/10.1016/j.conbuildmat.2019.116986.
Ma, H., Zhou, P., Qian, J., Deng, Y., Shi, Y., Lian, B., 2025. Evolution of gas seepage properties in shale fractures under different confining pressure and temperature conditions. Int. Commun. Heat Mass Tran. 165, 109039. https://doi.org/10.1016/j.icheatmasstransfer.2025.109039.
McMahon, T.P., Larson, T.E., Zhang, T., Shuster, M., 2024. Geologic characteristics, exploration and production progress of shale oil and gas in the United States: an overview. Petrol. Explor. Dev. 51 (4), 925–948. https://doi.org/10.1016/S1876-3804(24)60516-1.
Nemčok, M., Doré, A.G., Henk, A., Doran, H., 2025. Models of hydrocarbon migration. In: Strike-Slip Terrains and Transform Margins Structural Architecture, Thermal Regimes and Petroleum Systems. Cambridge University Press, pp. 589–617. https://doi.org/10.1017/9781108686631.018.
Paul, A., Mukherjee, S., Biswas, M., 2025. Global review on shale: focus on hydrocarbon geoscience & carbon sequestration. Results in Earth Sciences 3, 100088. https://doi.org/10.1016/j.rines.2025.100088.
Pik, I., Golubev, N., Kaidalov, A., Kann, J., Elenurm, A., 2001. Current status of oil shale processing in solid heat carrier UTT (Galoter) retorts in Estonia. Oil Shale 18 (2), 99–107. https://doi.org/10.3176/oil.2001.2.02.
Qi, J., Sui, W., Zhang, G., Xu, J., 2014. Calculation and analysis of the porosity and fractal dimension of red stratum sandstone based on SEM images processing. J. Eng. Geol. 22 (s1), 339–345. https://doi.org/10.13544/j.cnki.jeg.2014.s1.057 (in Chinese).
Rouquerol, J., Avnir, D., Everett, D.H., Fairbridge, C., Haynes, M., Pernicone, N., Ramsay, J.D.F., Sing, K.S.W., Unger, K.K., 1994a. Guidelines for the characterization of porous solids. Stud. Surf. Sci. Catal. 87, 1–9. https://doi.org/10.1016/S0167-2991(08)63059-1.
Rouquerol, J., Avnir, D., Fairbridge, C.W., Everett, D.H., Haynes, J.M., Pernicone, N., Ramsay, J.D.F., Sing, K.S.W., Unger, K.K., 1994b. Recommendations for the characterization of porous solids (Technical Report). Pure Appl. Chem. 66 (8), 1739–1758. https://doi.org/10.1351/pac199466081739.
Silva, G., de Miranda, F.P., Michelon, M., Ovídio, A., Venturelli, F., Parêdes, J., Ferreira, J., Moraes, L., Barbosa, F., Cury, A., 2025. A comparative study of fractal models applied to artificial and natural data. Fractal and Fractional 9 (2), 87. https://doi.org/10.3390/fractalfract9020087.
Sing, K.S.W., 1982. Reporting physisorption data for gas/solid systems with special reference to the determination of surface area and porosity (Provisional). Pure Appl. Chem. 54 (11), 2201–2218. https://doi.org/10.1351/pac198254112201.
Sing, K.S.W., 1985. Reporting physisorption data for gas/solid systems with special reference to the determination of surface area and porosity (recommendations 1984). Pure Appl. Chem. 57 (4), 603–619. https://doi.org/10.1351/pac198557040603.
Su, Y.L., Xu, J.L., Wang, W.D., Wang, H., Zhan, S.Y., 2022. Relative permeability estimation of oil-water two-phase flow in shale reservoir. Pet. Sci. 19 (3), 1153–1164. https://doi.org/10.1016/j.petsci.2021.12.024.
Syed, F.I., Dahaghi, A.K., Muther, T., 2022. Laboratory to field scale assessment for EOR applicability in tight oil reservoirs. Pet. Sci. 19 (5), 2131–2149. https://doi.org/10.1016/j.petsci.2022.04.014.
Tian, S., Zhou, J., Xian, X., Gan, Q., Zhang, C., Dong, Z., Kuang, N., 2023. The impact of supercritical CO2 exposure time on the effective stress law for permeability in shale. Energy 284, 129334. https://doi.org/10.1016/j.energy.2023.129334.
Wang, B.Y., Cao, R.Y., Zheng, X.Y., Cheng, L.S., Hu, J.P., Jia, Z.H., Duan, W.H., Hassanzadeh, H., 2025. Real-time NMR experimental study of displacement–imbibition coupling in tight/shale oil reservoirs: lithological variations, influencing factors, and key insights. Pet. Sci. 22 (12), 5142–5165. https://doi.org/10.1016/j.petsci.2025.08.028.
Wang, G., Jin, Z., Liu, G., Wang, R., Zhao, G., Tang, X., Liu, K., Zhang, Q., 2023. Pore system of the multiple lithofacies reservoirs in unconventional lacustrine shale oil formation. Int. J. Coal Geol. 273, 104270. https://doi.org/10.1016/j.coal.2023.104270.
Wang, G., Yin, Q., Jia, H., Feng, G., Liu, S., Heng, S., 2026. Experimental study on anisotropic pore-fracture and real-time permeability evolution of fractured oil shale under high temperature and triaxial stress: a case study of Jimsar oil shale in Xinjiang, China. Rock Mech. Rock Eng. 59, 183–205. https://doi.org/10.1007/s00603-025-04725-z.
Wang, L., Zeng, X., Yang, H., Lv, X., Guo, F., Shi, Y., Hanif, A., 2021. Investigation and application of fractal theory in cement-based materials: a review. Fractal and Fractional 5 (4), 247. https://doi.org/10.3390/fractalfract5040247.
Wang, W., Lin, C., Zhang, X., 2024. Fractal dimension analysis of pore throat structure in tight sandstone reservoirs of Huagang Formation: jiaxing Area of East China Sea Basin. Fractal and Fractional 8 (7), 374. https://doi.org/10.3390/fractalfract8070374.
Wang, Z., Yao, J., Sun, H., Yan, X., Yang, Y., 2021. A multi-continuum model for simulating in-situ conversion process in low-medium maturity shale oil reservoir. Adv. Geo-Energy Res. 5 (4), 456–464. https://doi.org/10.46690/ager.2021.04.10.
Wu, J., Zhang, C., Yu, B., Yin, S., Xing, M., Chen, X., Lian, H., Yi, S., 2022. Fractal characteristics of low-permeability sandstone reservoirs. Fractals: An interdisciplinary journal on the complex geometry of nature 30 (4), 2250075. https://doi.org/10.1142/S0218348X2250075X.
Wu, S., Yang, Z., Zhai, X., Cui, J., Bai, L., Pan, S., Cui, J., 2019. An experimental study of organic matter, minerals and porosity evolution in shales within high-temperature and high-pressure constraints. Mar. Petrol. Geol. 102, 377–390. https://doi.org/10.1016/j.marpetgeo.2018.12.014.
Xiao, J., Lv, Z., Duan, Z., Zhang, C., 2023. Pore structure characteristics, modulation and its effect on concrete properties: a review. Constr. Build. Mater. 397, 132430. https://doi.org/10.1016/j.conbuildmat.2023.132430.
Xiao, M., Wang, X., Hou, Z., Alan Quezada Renteria, J., Dlamini, D.S., Jassby, D., Hoek, E.M.V., 2025. Comparison of classical hydrodynamic models of transport through porous membranes. Separation and Purification Technology 360, 131189. https://doi.org/10.1016/j.seppur.2024.131189.
Xie, B.C., Wanke, P.F., Wang, H., Chen, X.-P., 2026. Environmental assessment of energy structure transition. Environ. Impact Assess. Rev. 117, 108181. https://doi.org/10.1016/j.eiar.2025.108181.
Xie, J., Zhao, Y., 2017. Meso-mechanism of permeability decrease or fluctuation of coal and rock with the temperature increase. Chin. J. Rock Mech. Eng. 36 (3), 543–551. https://doi.org/10.13722/j.cnki.jrme.2016.0226 (in Chinese).
Xu, S., Sun, Y., Yang, Q., Wang, H., Kang, S., Guo, W., Shan, X., He, W., 2023. Product migration and regional reaction characteristics in the autothermic pyrolysis in-situ conversion process of low-permeability Huadian oil shale core. Energy 283, 128525. https://doi.org/10.1016/j.energy.2023.128525.
Xu, Y., Lun, Z., Pan, Z., Wang, H., Zhou, X., Zhao, C., Zhang, D., 2022. Occurrence space and state of shale oil: a review. J. Petrol. Sci. Eng. 211, 110183. https://doi.org/10.1016/j.petrol.2022.110183.
Yan, X., Huang, Z., Lun, Z., Fu, J., Zhang, T., Zhao, C., Wang, H., Xie, Y., Fan, C., Zhang, D., Zou, J., 2026. Retention of fracturing fluid in shale oil formations based on 1D- and 2D-NMR: implications to shale oil production. Fuel 406, 136870. https://doi.org/10.1016/j.fuel.2025.136870.
Yang, L., Yang, D., Zhao, J., Liu, Z., Kang, Z., 2016. Changes of oil shale pore structure and permeability at different temperatures. Oil Shale 33, 101–110. https://doi.org/10.3176/oil.2016.2.01.
Yang, X., Liu, J.-Y., 2025. Fractal dynamics modeling of spatiotemporal pore structure evolution in tight reservoirs. Fractal and Fractional 9 (12), 760. https://doi.org/10.3390/fractalfract9120760.
Zhang, L., Lu, S., Jiang, S., Xiao, D., Chen, L., Liu, Y., Zhang, Y., Li, B., Gong, C., 2018. Effect of shale lithofacies on pore structure of the Wufeng-Longmaxi shale in the southeast Chongqing, China. Energy & Fuels 32 (6), 6603–6618. https://doi.org/10.1021/acs.energyfuels.8b00799.
Zhang, L., Xu, Y., Sun, M., Jiang, S., Zhang, Y., Wu, C., Zhang, J., Liang, X., Wang, G., 2021. The structure and evolution of closed pores in shale determined by small angle neutron scattering. Acta Sedimentol. Sin. 39 (2), 310–323. https://doi.org/10.14027/j.issn.1000-0550.2020.111 (in Chinese).
Zhang, W., Lan, S., Ma, W., Wang, J., 2023. Study on the evolution of pore structure characteristics of Xinjiang oil shale during the heating progress. J. Jilin Univ. (Earth Sci. Ed.) 53 (6), 1689–1705. https://doi.org/10.13278/j.cnki.jjuese.20230033 (in Chinese).
Zhang, Y., Wang, L., Yang, D., Zhang, X., Huang, X., Kang, Z., 2025. Study on the construction of 3D complex pore networks and the dynamic evolution of seepage pathways in oil shale during in-situ pyrolysis by convective heating. Energy 333, 137276. https://doi.org/10.1016/j.energy.2025.137276.
Zhang, Z., Montilla, M.J.B., Xie, Z., Li, S., Hu, Y., Li, X., 2024a. Comparative analysis of wellbore electrical heating, low-frequency heating, and steam injection for in-situ conversion in continental shale oil reservoirs. Case Stud. Therm. Eng. 64, 105512. https://doi.org/10.1016/j.csite.2024.105512.
Zhang, Z., Zhang, Z., Lu, W., Guo, H., Liu, C., Ning, F., 2024b. Pore-scale investigations of permeability of saturated porous media: pore structure efficiency. J. Hydrol. 637, 131441. https://doi.org/10.1016/j.jhydrol.2024.131441.
Zhao, J., Kang, Z., 2021. Permeability of oil shale under in situ conditions: fushun oil shale (China) experimental case study. Natural Resources Research 30, 753–763. https://doi.org/10.1007/s11053-020-09717-0.
Zhou, X., Li, L., Lei, Z., Su, Y., Tang, J., You, C., Liu, S., Li, M., 2026. Relative permeability model of oil-water flow in shale considering nanoconfinement and shape effects. SPE J. 31 (3), 1896–1914. https://doi.org/10.2118/231826-PA.
Zhu, B., Guo, W., Sun, Y., Deng, S., Zhu, C., Liu, H., Li, Q., 2026. Field experiment study of well-group control and exploitation in Fuyu oil shale using topochemical heat in-situ conversion technology. Fuel 416, 138562. https://doi.org/10.1016/j.fuel.2026.138562.
Zhu, C.F., Zhang, T.L., Pan, J.F., Li, Y.W., Sheng, J.J., Ge, D., Jia, R., Guo, W., 2025. Evolution of the 3D pore structure of organic-rich shale with temperature based on micro-nano CT. Pet. Sci. 22 (6), 2339–2352. https://doi.org/10.1016/j.petsci.2025.03.037.
Zou, C., Lin, M., Ma, F., Liu, H., Yang, Z., Zhang, G., Yang, Y., Guan, C., Liang, Y., Wang, Y., Xiong, B., Yu, H., Yu, P., 2024. Development, challenges and strategies of natural gas industry under carbon neutral target in China. Petrol. Explor. Dev. 51 (2), 476–497. https://doi.org/10.1016/S1876-3804(24)60038-8.